Hydrodynamic simulations of He-shell flash convection

Falk Herwig[1], Bernd Freytag[1] [2] [3], Robert M. Hueckstaedt[1], Francis X. Timmes[1]

ABSTRACT

We present the first hydrodynamic, multi-dimensional simulations of He-shell flash convection. Specifically, we investigate the properties of shell convection at a time immediately before the He-luminosity peak during the 15th thermal pulse of a stellar evolution track with initially two solar masses and metallicity $Z = 0.01$. This choice is a representative example of a low-mass asymptotic giant branch thermal pulse. We construct the initial vertical stratification with a set of polytropes to resemble the stellar evolution structure. Convection is driven by a constant volume heating in a thin layer at the bottom of the unstable layer. We calculate a grid of 2D simulations with different resolutions and heating rates. Our set of simulations includes one low-resolution 3D run. The computational domain includes 11.4 pressure scale heights. He-shell flash convection is dominated by large convective cells that are centered in the lower half of the convection zone. Convective rolls have an almost circular appearance because focusing mechanisms exist in the form of the density stratification for downdrafts and the heating of localized eddies that generate upflows. Nevertheless, downdrafts appear to be somewhat more focused. The He-shell flash convection generates a rich spectrum of gravity waves in both stable layers above and beneath the convective shell. The magnitude of the convective velocities from our 1D mixing-length theory model and the rms-averaged vertical velocities from the hydrodynamic model are consistent within a factor of a few. However, the velocity profile in the hydrodynamic simulation is more asymmetric, and decays exponentially inside the convection zone. An analysis of the oscillation modes shows that both g-modes and convective motions cross the formal convective boundaries, which leads to mixing across the boundaries. Our resolution study shows consistent flow structures among the higher resolution runs, and we see indications for convergence of the vertical velocity profile inside the convection zone for the highest resolution simulations. Many of the convective properties, in particular the exponential decay of the velocities, depend only weakly on the heating rate. However, the amplitudes of the gravity waves increase with both the heating rate and the resolution.

Subject headings:

1. Introduction

We present hydrodynamic simulations of the interior shell convection zone driven by the He-shell flash in thermal pulse Asymptotic Giant Branch (AGB) stars.

[1]Los Alamos National Laboratory, Los Alamos, NM 87544, e-mail: fherwig/rmhx/timmes@lanl.gov

[2]Department of Astronomy and Space Physics at Uppsala University, Sweden, e-mail: bf@astro.uu.se

[3]Department of Physics and Astronomy, Michigan State University, East Lansing, MI 48824

1.1. AGB evolution

AGB stars are the final evolution stage of low- and intermediate mass stars before formation of a white dwarf (Iben & Renzini 1983). Nuclear production in AGB stars contribute to the chemical evolution of galaxies (for example Travaglio et al. 2004; Renda et al. 2004). The chemical yields are support the interpretation stellar abundance from dwarf-spheroidal galaxy satellites of the Milky Way relative to stellar abundances of galactic halo stars (Venn et al. 2004; Geisler et al. 2005). This may provide important clues about

the cosmological origin of our galaxy. Another role of AGB stars have recently been discussed as a potential source of the abundance anomalies observed in globular cluster star members (Ventura et al. 2002; Denissenkov & Herwig 2003), a question that is still debated.

AGB stars produce substantial amounts of Li, C, N, ^{22}Ne, ^{23}Na, and the neutron-heavy Mg isotopes. These stars are the progenitors of planetary nebulae nuclei and white dwarfs, including those thought to orbit C-rich extremely metal-poor stars with s-process signature (CEMP-s, Beers & Christlieb 2005). The favoured interpretation of their strongly non-solar abundance pattern is the pollution of the EMP star with material transfered from the white dwarf progenitor AGB star. This interpretation is largely based on the fact that the abundance patterns of CEMP-s stars in general resemble the C- and s-process overabundance predicted for EMP AGB stars. However, very significant discrepancies between observed and predicted abundances exist which could indicate some serious problem with current 1D stellar evolution and nucleosynthesis simulations. Most likely those problems are related to the 1D approximate treatment of mixing that originate from multi-dimensional, convective fluid motions.

Especially at extremely low metallicity, AGB stars can produce many species in a primary mode, i.e. only with the H and He available from the Big Bang (Siess et al. 2002; Herwig 2004, for example). AGB stars are also the nuclear production site of the main component of the s process (Busso et al. 1999), which produces roughly half of all trans-iron elements (Arlandini et al. 1999). The interpretation of high-precision laboratory measurements of isotopic ratios of heavy elements in presolar meteoritic SiC grains depends sensitively on the thermodynamic and the closely related mixing conditions at the bottom of the He-shell flash convection zone (Zinner 1998; Lugaro et al. 2003a,b). In this particular layer the ^{22}Ne$(\alpha, n)^{25}$Mg reaction releases neutrons very rapidly, and activates many s-process branchings. Experimental measurements of nuclear properties of the unstable branch-point nuclei are now underway (Reifarth et al. 2005) and in conjunction with grain measurements will provide new constraints for mixing at convective boundaries in the future.

Currently, only 1D stellar evolution models exist to describe the processes of the AGB stellar interior quantitatively. However, while spherical symmetry is globally a very good approximation, a detailed description of mixing processes induced by the hydrodynamic fluid-flows requires multi-dimensional simulations. Only over long times, equivalent to many convective turn-overs, can they be described accurately by the average quantities provided by the commonly used local theories, like the mixing-length theory (Böhm-Vitense 1958). However, it is well known that these theories do not describe the quantitative properties of mixing at convective boundaries. For these reasons, we start our investigations of the hydrodynamic properties of stellar interior convection with the He-shell flash convection in thermal pulse AGB stars.

1.2. Hydrodynamic simulations of stellar convection and application to 1D stellar evolution calculations

Most multi-dimensional simulations of stellar convection address the outer convection zones. For example the solar convection zone including the surface granulation (Nordlund 1982; Stein & Nordlund 1998), convection below the surface (Stein & Nordlund 1989) or the role of magnetic fields and rotation in the solar convection zone (Brun 2004) Other simulations include work on deep envelope convection in giants (Porter & Woodward 1994, 2000; Freytag et al. 2002; Robinson et al. 2004), shallow surface convection, for example in A stars and white dwarfs (Freytag et al. 1996) and the general properties of slab convection (Hurlburt et al. 1986). Hydrodynamic simulations of stellar interiors include an investigation of semi-convection in massive stars by Merryfield (1995) and core convection in rotating A-type stars (Browning et al. 2004).

The work by Freytag et al. (1996) motivated Herwig et al. (1997) to include the exponential overshooting derived from hydrodynamical simulations to all convective boundaries. The e-folding distance for convective boundaries in the stellar interior was derived semi-empirically for main-sequence stars, and then applied to AGB stars (Herwig 2000). Similar approaches were considered by Mazzitelli et al. (1999), Ventura et al. (2000), Cristallo et al. (2004), and Althaus et al. (2005).

However, convection in shells driven by nuclear energy release is different than envelope convection. Typically, the Mach numbers are smaller throughout the convection zone, and the bordering radiative layers are relatively more stable. Accordingly, the semi-empirical determination of the overshooting value f_{ov}[4] gives smaller values for the stellar interior ($f_{OV} < 0.016$) compared to the shallow surface convection ($0.25 < f_{OV} < 1.0$) according to Freytag et al. (1996). For deep envelope (or core) convection f_{ov} can be expected to be considerably smaller since the ratio of the Brunt-Väisälä time-scales of the stable to the unstable layers decrease with increasing depth, i.e. adiabaticity (Herwig et al. 1997).

Relevant in this regard are the 2D simulations of interior O-burning shell convection in massive stars immediately before a supernova explosion of Bazan & Arnett (1998) and Asida & Arnett (2000). In these simulations hydrodynamic fluid motions are not confined to the convectively unstable region. The authors describe the excitation of gravity waves in the adjacent stable layers (Hurlburt et al. 1986), as well as an exponential decay of convective velocities at and beyond the convective border. As a result highly reactive fuel in the form of C is mixed from above into the O-shell. However, the authors caution that the quantitative results may suffer some uncertainty due to numerical effects like resolution. The main difference between these simulations and our regime of the He-shell flash is the lower driving energy in our case, and we expect correspondingly lower Mach numbers, less mixing and less overshooting. Young et al. (2005) present initial results on updated O-shell 2D and 3D convection simulations and apply their findings on hydrodynamics mixing to 1D stellar evolution models of supernova progenitors (Young & Arnett 2005). The internal structure in these models is markedly different from standard models, with important implication for the supernova explosion properties.

---

[4]Here, the overshoot formulation is $D_{OV} = D_0 \exp\left(\frac{-2z}{f_{ov} \cdot H_p}\right)$, where D_0 is the mixing-length theory mixing coefficient at the base of the convection zone, z is the geometric distance to the convective boundary, H_p is the pressure scale height at the convective boundary, and f_{ov} is the overshooting parameter (Herwig et al. 1997).

1.3. About this paper

The main purpose of our study is to obtain a characterization of the hydrodynamic properties of shell convection in low-mass stars which is determined by weaker driving due to smaller nuclear energy generation compared to massive stars. We investigate the typical morphology, the dominating structures and the time-scales of shell-flash convection, and how these properties depend on resolution and driving energy. We identify areas of parameter space that require further study in two- and three-dimensions. In our present work we do not intend to quantify mixing across the convective boundary, but we want to gain insight for future simulations that shed more light on this important question.

In the following section we describe the 1D stellar evolution code and the hydrodynamics codes used in this work. Sect. 3 describes the stellar evolution sequence and the specific model that serves as a template for the hydrodynamic simulations. Then we describe the results in Sect. 4; specifically we describe the general properties of the convection, the onset of convection, the evolved convection and the convective and oscillation modes observed in our simulations. We close the paper with a discussion (Sect. 5) of the results, in particular the comparison of the 1D MLT velocity profile and the time-averaged vertical velocity profile from our hydrodynamic simulations.

2. Codes

2.1. Stellar evolution code

Our 1D hydrostatic, Lagrangian stellar evolution code EVOL with adaptive mesh refinement and time stepping is equipped with up-to-date input physics (Herwig 2004, and references therein). Mass loss is included according to the formula given by Blöcker (1995) with a scaling factor $\eta_{BL} = 0.1$. Nucleosynthesis is considered by solving a sufficiently detailed nuclear network, with reaction rates from the NACRE compilation (Angulo et al. 1999). We use OPAL opacities (Iglesias & Rogers 1996) and low-temperature opacities from Alexander & Ferguson (1994). In the stellar evolution code convective energy transport is described by the mixing-length theory (Böhm-Vitense 1958) with a constant mixing length pa-

rameter of $\alpha_{\mathrm{MLT}} = 1.7$ determined by calibrating a solar model with the parameters of the sun. For material mixing we solve a diffusion equation for each species with a convective diffusion coefficient as given by Langer et al. (1985).

2.2. Hydrodynamics code

For the hydrodynamic simulations we use the multi-dimensional radiation-hydrodynamics code RAGE (Radiation Adaptive Grid Eulerian) designed to model a variety of multi-material flows (Baltrusaitis et al. 1996). The conservation equations for mass, momentum, and total energy are solved through a second-order, direct-Eulerian Godunov method on a finite volume mesh (Dendy & Gittings 2005). RAGE has been extensively tested on verification problems (Belle et al. 2005; Holmes et al. 1999; Hueckstaedt et al. 2005). The code has the capability for continuous adaptive-mesh refinement to increase spatial resolution in areas of interest with a minimal increase in computational time. This capability is in particular useful for multi-fluid applications. We do not use this feature because all our runs have a single-fluid.

3. Stellar evolution models of the He-shell flash and initial multi-dimensional setup

We simulate the He-shell convection zone at a time point during a thermal pulse evolution immediately before the peak of the He-luminosity. At this time the He-burning luminosity that drives the convection is already large implying a rapid build-up of an entropy excess that drives convection. At the same time the layer has not yet been expanded too much, and the number of pressure scale heights involved is not excessive. Nevertheless, our simulations vertically span $11.4\mathrm{H_p}$. Our inital conditions are a a set of polytropic profiles that closely resembles the structure from the full 1D stellar evolution model.

3.1. The stellar evolution model

Our hydrodynamic simulations are based on a model from run ET2 of Herwig & Austin (2004) that represents typical properties of a thermal pule in a low-mass asymptotic giant branchn star. This sequence has metallicity $Z = 0.01$ and the main-sequence initial mass is $2\,\mathrm{M_\odot}$. The evolution track

was followed from the pre-main sequence until all envelope mass was lost at the tip of the AGB. We assumed exponential, time- and depth-dependent overshooting at the bottom of the convective envelope ($f_{\mathrm{ov}} = 0.016$). At the bottom of the He-shell flash convection zone a very small overshooting ($f_{\mathrm{ov}} = 0.001$) was applied, mainly for numerical reasons. Such a small overshooting value has little noticeable effect on the evolution but improves the convergence of the code. The diffusion coefficient drops 5 orders of magnitude within only 7 grid points corresponding to about 7km, or less than $0.01\mathrm{H_p}$. Sequence ET2 has 16 thermal pulses, eight of which are followed by a third dredge-up.

We choose a model from the second to last (15th) thermal pulse of the ET2 run. At this thermal pulse, the core mass is $0.6\,\mathrm{M_\odot}$ and the entire stellar mass is $1.4\,\mathrm{M_\odot}$. For a stellar model as template for the initial stratification of the hydrodynamic simulations, we favor a large luminosity which implies large convective velocities. However, the large luminosity quickly leads to a significant expansion of the layers above the He-shell (Fig. 1), which dramatically increases the number of pressure scale heights that the simulation would have to cover (Fig. 2). In particular, we would like to include enough stable layer above and below the convection zone to get an impression of the hydrodynamic fluid behavior at the convective boundaries and the adjacent stable regions.

We picked model 70238 of that rerun as a template for our hydrodynamic initial setup. This model is one time-step (0.07 yr) before the peak of the He-shell flash luminosity of $4.29 \cdot 10^7\,\mathrm{L_\odot}$ (model 70239). The thermodynamic and mixing properties of model 70238 are given in Table 1 for the top and bottom of the convection zone and the location of where we chose the top and bottom of the hydrodynamic simulation box to be. The simulations covers a total $11\,\mathrm{H_p}$, roughly half of this inside the convection zone.

The molecular weight profile and the convective velocity $v_{\mathrm{conv}} = D/(\frac{1}{3}\alpha_{\mathrm{MLT}}H_{\mathrm{P}})$ are shown for two consecutive models (70237 and 70238) in Fig. 3 and 4. The time step between the two models is 0.04 yr corresponding to approximately 1400 convective turnovers. The radius integrated He-burning energy in the two subsequent models 70237 and 70238 is $4.7 \cdot 10^{17}$ and $1.1 \cdot 10^{18}\mathrm{cm\,erg/g/s}$. During the He-shell flash, the

nuclear energy is mainly generated by the triple-α reaction.

3.2. The hydrodynamic simulation setup and run parameters

We simulate a plane-parallel layer in Cartesian coordinates which represents the intershell of the AGB star at the time nearly at the peak He-shell flash luminosity. In our models (lc0 for 2D and lc1 for 3D), the grid is equidistant in all dimensions, with a cell size of 55km in our standard mesh g (600x200). The box covers 33000km horizontally and 11000km vertically in the 2D runs.

The bottom of the simulation box is located at a stellar model radius of 7507.5km, and subsequently all length scales are with reference to the box bottom. The bottom of the convection zone is at 1650km. We approximate the stellar evolution model stratification in the simulation box by a combination of three polytropic stratifications (Hurlburt et al. 1986), with γ in each layer approximating the γ in the corresponding layer in the stellar evolution model. For the region below the convection zone we assume a stable polytropic stratification with $\gamma = 1.2$. For the convective region we set $\gamma = \gamma_{ad} = 5/3$, while the top polytropic stable stratification mimics the stellar model with $\gamma = 1.01$. At the bottom of the convection zone we set the temperature to $2.48 \cdot 10^8$ K and the density to $1.174 \cdot 10^4 g/cm^3$ as in the stellar model(see Fig. 6). We fix the temperature below the convection zone and at the top of the lower stable layer at $1.17 \cdot 10^8$ K, corresponding to a factor of 0.47 between the peak temperature at the bottom of the convection zone and the local temperature minimum just below the convection zone. The location of the top of the convection zone is set to 7732.4km from the bottom of the box, corresponding exactly to the value in the stellar model. The top of the box at 11000km from the box bottom is chosen to be just below the H-rich envelope. Fig. 6 demonstrates the agreement between our piecewise polytropic stratification and the stellar evolution template model.

In the RAGE code the molecular weight of a material is specified in terms of the specific heat, which for an ideal gas is $c_V = \frac{3}{2}\frac{\mathcal{R}}{\mu}$, with the universal gas constant $\mathcal{R} = 8.31 \cdot 10^7 erg/K/g$. $\mu-$gradients are present at the bottom and top of

the convection zone (Fig. 3). Although they add stability and reduce mixing across the boundaries, we ignore $\mu-$gradients in this set of calculations. We plan to address the effect of μ-gradients in a future study. Here, we chose as a single mean molecular weight $\mu = 1.4$ which closely matches the value in the convection zone from the stellar model. Finally, we assume a constant gravity of $\log g = 7.7$[cgs] vertically directed downward as in the convection zone of the stellar model. In the stellar model gravity varies from $\log g = 8.05$ at the bottom of the simulated layer to $\log g = 7.35$ at the top.

In the stellar evolution model, the nuclear energy that drives the convection is calculated by solving a nuclear network based on realistic temperature-dependent nuclear reaction rate input. The same approach used in the hydrodynamic calculation may introduce additional resolution dependencies of localized flow morphologies, in particular at the bottom of the convection zone. We assume here a time-, temperature- and resolution-independent volume heating in a small layer at the bottom of the convection zone that releases the same integrated amount of energy as the stellar evolution model. Specifically, we release approximately $\epsilon_0 = 2 \cdot 10^{10} erg/g/s$ over 550km at the bottom of the adiabatic stratification. A constant volume heating is realized by multiplying ϵ_0 with the density at the bottom of the convection zone for the input value ($\epsilon^\star = \epsilon_0\rho_0$) and then locally in each cell adding $\epsilon = \epsilon^\star/\rho$ to the cell energy.

We introduce random density and temperature perturbations in pressure equilibrium on the grid-level of $\log \Delta T/T = -4$ and centered at the unperturbed values. Due to the discretization error, the initial numerical stratification slightly violates hydrostatic equilibrium. This would cause a spectrum of plane-parallel p-mode oscillations with significant velocity amplitudes. During an initial damping phase (700s) of the simulations we damp those artificial p-modes to amplitudes at the cm/s-level. The damping is achieved by multiplying a factor to the momentum in each cell. This damping factor decreases from an initial value to zero over the damping phase. A corresponding heating factor increases from 0 to 1 over the damping phase and smoothly turns heating for convection driving on. The length of the damping phase

was chosen so that an overall velocity minimum could be achieved before the onset of convective motions.

We formulated a grid of runs in 2D that cover a range in resolution and heating rate (Fig. 5). These runs are labeled lc0AB, where lc = luminosity driven convection, 0 is the run series, in this case a series of 2D runs, A denotes the heating rate and B the grid size. We have done one 3D run, denoted by lc1. We also discuss two runs (lc2) in which we have used three formally different species in the three layers of our setup, but the three materials have the same material properties. This allows some preliminary insight into mixing.

3.3.   Time-scales and summary

The convective turn-over time scale is of the order of 600s and convective velocities are of the order a few km/s. We use an explicit, compressible hydrodynamics code, in which the time step is limited by the Courant-Friedrichs-Levy condition imposed by the sound speed. The maximum sound speed in our setup is > 1000km/s. Accordingly, our convective flows have a low Mach number of the order 10^{-3}Ma. With a grid size of 55km this implies a time step of $\Delta t < 5 \cdot 10^{-2}$s. In order to achieve some convective steady-state and evolve this configuration for some time to have good statistics, our multi-dimensional simulations run for approximately 15 to 30 convective turn-over times, which corresponds to more than 10^5 time steps. Thus, the multi-dimensional simulation time is much less than 0.1% of the stellar evolution calculation time-step that reflects the thermal time scale. Our calculation represent a snapshot in time compared to the long-term evolution of the entire He-shell flash which takes $200 - 300$ yr. In our simulations we assume a constant heating rate in time. For the highly adiabatic He-shell flash convection the ratio between convective and non-convective heat transport (the Peclet number) is very large. For that reason we ignore thermal transport in this set of simulations.

By running a series of simulations with heating rates spanning a factor 1000 we study how hydrodynamic properties depend on the heating rate. We also want to derive how our results depend on resolution. Fig. 5 gives an overview of our 2D runs for our standard single-fluid setup lc0.

4.   Results

Our simulations start with a Raleigh-Taylor like growth sequence of the initial perturbations driven by the heating at the bottom of the unstable layer (Sect. 4.1). Eventually, fully developed convection emerges (Sect. 4.3). It features a cellular flow configuration best seen in the pseudo-streamline plot in Fig. 7. The flow field is dominated by a few large cells (about 4 in that example) each consisting of a clockwise and a counter-clockwise vortex. Vertically the cells span the entire convectively unstable region. However, the vortex centers are located closer to the bottom, and leave room for some substructure in the top layers of the convectively unstable zone. Additional smaller rolls also appear close to the bottom boundary. Gravity waves are excited in the stable layers. An oscillaton mode analysis of the their appearance at the transition from unstable to stable stratification can be used to better understand the interaction of stable and unstable layers (Sect. 4.5). Fig. 8 shows the corresponding entropy fluctuations for the same snapshot. Hot material rises from the heating layer at the bottom of the convection zone. The bulk of the high-entropy areas starts to turn side-ways well below the top of the unstable layer. However vertical high-velocity streams persist through the unstable layer, and the velocity field can be perpendicular to the streaks of high-entropy material.

4.1.   Onset of convection

The drag force applied in the first 700 s (p-mode filter, Sect. 3.2) of a simulation eliminates efficiently all modes that appear due to the imperfect hydrostatic equilibrium of the initial stratification. On the other hand, it also delays the onset of convection somewhat.

After some time, the external heating builds up a small extra entropy bump at the bottom of the entropy plateau. The top of this bump is the place where the entropy has the steepest negative slope, and where the convective instability causes small-scale modes to grow first (see the top panel in Fig. 9). The modes expand vertically and the velocity amplitude increases. Later, when they leave the linear regime, they form a patch of tiny mushroom-like instabilities that are similar in their morphology to the Raleigh-Taylor instability. These grow and merge further forming

complex large-scale structures (Fig. 9).

The stable regions are far from being quiet but instead filled with waves. Remarkably, these waves occur in the upper stable zone well before the convective plumes reach this layer. The motions are not excited by plumes "hitting" the boundary layer but by the pressure excess in front of the plumes. This can be clearly seen in Fig. 10 which shows the pressure fluctuations and pseudo-streamlines of the same time and model as the middle panel of Fig. 9. The rising plumes have not yet reached the top of the unstable layers; however the entropy fluctuations at and above the top of the unstable layer show that oscillation modes are already excited by the fluctuating over-pressure regions seen, for example, at the horizontal position $x=25\,\mathrm{Mm}$ in Fig. 10. We demonstrate in Sect. 4.5 that these oscillation modes are in fact gravity waves.

Figure 12 demonstrates that the amount of detail visible in the plumes strongly depends on the resolution while the number of plumes (or the size of the largest structures at a given time-step) is only slightly affected. The wavelength of the modes that initially start to grow and also the size of the first generation of mushrooms decreases with grid size. However, these small-scale structures quickly merge to form much larger cells.

We do not present models with a coarser grid than 210x70 because test runs have shown that numerical problems arise at the upper boundary of the box (an artificial entropy inversion and tiny "surface cells"). That is not particular worrisom; a hydrodynamics code needs a minimum number of grid cells to resolve a pressure scale height properly, and we have about $11.4\,\mathrm{H_p}$ inside our box.

In the low-resolution model (top panel in Fig. 12) the entropy above the "mushrooms" is not constant as it should be for perfectly adiabatic flows. This artifact essentially vanishes with increasing resolution and does not seem to have any adverse effect.

To demonstrate the influence of the heating rate upon the convective patterns during the onset phase, a scaling of the amplitude of the entropy inhomogeneities (the fluctuations increase with the heating) and adjustment of the selected time-steps are necessary (a larger heating rate causes larger convective velocities and shorter growth times,

see Fig. 13). Taking the scaling into account, the resulting morphology of the convective flows are remarkably similar, suggesting the possibility of avoiding excessively CPU-intensive simulations with low heating rates and correspondingly small convective velocities.

Careful inspection of the lower panels of Fig. 13 reveals spurious entropy minima as dark spots at the top of the entropy plateau caused by a small negative artificial entropy spike at that position. While the employed initial p-mode filter facilitates the relaxation to a complete numerical hydrostatic equilibrium, there is also a thermal relaxation going on with a much longer time-scale (hundreds of seconds instead of seconds). This process leads to a smearing of the initially sharp jump in density and internal energy at the bottom of the entropy plateau and in the discontinuity in the derivatives at the top of the plateau. This redistribution of density and energy does not preserve the entropy profile but causes an artificial (small) entropy maximum and minimum to occur at the bottom and the top of the entropy plateau, respectively. The amplitude and the width of the entropy spikes decrease with increasing resolution. However, at low resolutions and low (i.e. realistic) heating rates, they cause an initial driving of the convective flow comparable to the one due to the external heating.

Fortunately, this additional driving is a transient phenomenon because there is only a limited amount of energy available that can be "extracted" by a conservative code out of the discontinuities. It only increases the time it takes for the convection to settle to a statistically stationary state by approximately $3000\,\mathrm{sec}$ (for the run lc0gg) depending on resolution.

4.2. Onset of convection: 2D versus 3D

In addition to the two-dimensional models, we have some information from a single 3D run (lc1d, 1502x100 grid points). Figs. 14 and 15 display entropy inhomogeneities during the onset of convection for the 2D and the 3D run, respectively. Heating rate, vertical extent, and grid cell size are the same in both models.

The 3D model initially has smaller velocities and appears to be slightly behind the 2D model. However, as soon as convection sets in, the ve-

locities in the corresponding snapshots are very similar. The structures in the last panels seems to be slightly smaller in 3D than in 2D. However, distorted "mushrooms" appear in both sequences. Also, gravity waves are excited in both models.

We do not see any hint in the 3D models that would indicate that the results we derive from the grid of 2D models would suffer from the restriction to two dimensions. To get accurate quantitative results 3D models are to be preferred. However, 3D models with high resolution and realistically low heating rates are computationally extremely demanding. We will try to approach this regime in future work.

4.3. Evolved convection

We demonstrate the properties of fully developed convection by means of sequences of snapshots and averaged 1D profiles.

Figure 16 shows an example of the evolution of the convective patterns in a later stage of the 1200x400 run with realistic heating rate. During this time, the flow is dominated by 4 global cells (the aspect ratio of the unstable zone is about 6). The centers of the vortices are located in the lower half of this zone, characteristic for convection in a strongly stratified environment, as found by Hurlburt et al. (1984) in their stationary convection. However, in our case the upflows, starting in the thin heating layer at the bottom, are dynamic and change their shapes all the time. Smaller rolls can occur, especially at both sides of the foot-points of the updrafts and also near the top of the entropy plateau.

The stability of the general pattern is supported by the fact that the down-flows tend to inhibit the development of new updrafts that can develop due to the convective instability in the heated bottom layers. Instead, the heated material is pushed sideways into the existing upflow channels. During this process, new upflow "fingers" can develop. Most often, they are washed into the larger updrafts. However occasionally, they have a chance to grow and to change the global pattern.

The situation is pretty much the inverse of the well-known scenario of stellar surface convection, where radiative cooling creates a thin superadiabatic layer that leads to the formation of cool downdrafts that drive the convection. Whereas in surface convection the stratification tends to focus the downdrafts (Nordlund et al. 1997), the hot upflows expand. This expanding effect can widen the thin columns of hot upflowing material in the case of He-shell flash convection. Nevertheless, they can rise over several pressure scale heights before they break up and can traverse the entire convection zone.

The entropy jump at the bottom of the plateau and the sudden increase at the top (see Fig. 6) confine the convective flow essentially to the region in between – with very narrow transition layers. In these boundary layers the largest differences between the runs with different resolutions and heating rates occur. To compare them quantitatively, we compute some averaged quantities.

During the simulations a snapshot is stored every 0.5 s. This results for each quantity q (the velocity components, internal energy, ρ, T, P) in a data-set $q(x, y, t)$ depending on horizontal coordinate x, vertical coordinate y, and time t. This output high rate clearly over-samples the slow convective motions especially in the runs with low heating rates. However, it is justified for the fastest gravity waves. And it is just barely sufficient to sample the pressure waves (see Sect. 4.5).

For each snapshot we compute horizontal averages,

$$q_{\mathrm{avg}}(y, t) = \langle q(x, y, t) \rangle_x \qquad (1)$$

and horizontal root-mean-square (rms) fluctuations

$$q_{\Delta\mathrm{rms}}(y, t) = \left(\langle (q(x, y, t) - q_{\mathrm{avg}}(y, t))^2 \rangle_x \right)^{1/2} . \qquad (2)$$

We check the time evolution of these quantities to ensure that the simulations have reached a statistical steady state. Due to heating at the bottom of the convective layer the entropy of the convection zone is slowly increasing and the extent of the convection zone is growing at a small rate. The time evolution of the maximum vertical rms-velocity is shown for runs with standard and enhanced heating and different resolutions in Fig. 11. For the runs with the standard heating rate g a steady-state according to this disgnostic is reached after 6000s, following the onset phase of convection which is characterized by larger velocities. At a higher heating rate the difference between the initial velocity peak during the onset phase and the

following steady-state velocity is smaller. In this case the steady state is already reached after approximately 3000s.

To compare models with different resolutions or heating rates we average these quantities over time to get time-independent vertical profiles, as

$$q_{\mathrm{avg}}(y) = \langle q_{\mathrm{avg}}(y,t) \rangle_t \qquad (3)$$

or

$$q_{\Delta\mathrm{rms}}(y) = \left(\langle q_{\Delta\mathrm{rms}}(y,t)^2 \rangle_t \right)^{1/2} \quad . \qquad (4)$$

Examples for the rms-fluctuations of vertical and horizontal velocity are shown in Fig. 17, first and second row, respectively. Plotting the entropy s on the same scale as in Fig. 6 would show no difference to the initial stratification. Therefore, only the entropy difference to the minimum plateau value is plotted in the panels in the third row, on a highly magnified scale. To allow the comparison of models with very different heating rates (and entropy fluctuations) in the last row the same data is rescaled to give the entropy bump at the bottom of the plateau a value of unity.

The velocities are clearly not confined to the region that would have been predicted by MLT (between 1.7 Mm and 7.7 Mm, compare the top panels in Fig. 17 with Fig. 4). Nevertheless, before reaching the boundaries of the entropy plateau the vertical velocities drop exponentially by orders of magnitude. Close to the boundaries there are strong rapidly declining horizontal velocities leading to significant shear flows (second row of panels in Fig. 17).

Although the classical boundaries of a convection zone do not actually confine the velocity field completely, they still indicate where the flow changes its character: large overturning convective motions, inside and small wave-like motions outside (cf. Fig. 17 and e.g. Figs. 7 and 8). The low-heating models in Fig. 17 (top right panel) indicate the presence of a transition region where the velocities decline rapidly inside the top stable regions before they rise due to the waves.

The dependence of the velocity on the heating rate is rather simple: it grows monotonically with heating rate. The waves in the stable layers have larger amplitude than the velocities of the overturning convective motions (right column in Fig. 17). It is important to emphasize that the large vertical velocities shown in the stable lay-

ers of the top panels of Fig. 17 do not necessarily indicate effective mixing (see Sect. 4.6 for details).

The dependence on the resolution is somewhat similar. For the convective motions, there are hints towards convergence of the vertical and horizontal rms-velocities at the highest resolutions models (1200x400). However, the wave amplitude in the runs with large heating rate shows less convergence. The (logarithmic) step in the amplitude of the horizontal velocities between the 1200x400 and the 600x200 run is smaller than between the 600x200 and the 300x100 run. Models with even higher resolution are desirable to check the convergence. The appearence of similiar quantitative properties in He-shell flash convection appears to be robust; these properties are present at all resolutions and heating rates, in 2D and in 3D.

A higher resolution does not affect the number of large cells noticeably. However, it leads to finer entropy filaments and complex sub-structures of the largest plumes (cf. Figs. 18 and 19). Less numerical dissipation on a given scale leads to higher velocities, stronger velocity gradients (causing more dissipation), and some additional smaller rolls. However, even the high-resolution model in Fig. 7 shows the dominance of the large-scale structures. The trend to higher convective velocities is limited by the amount of energy that has to be transported.

The situation is different for the velocity amplitudes of the g-modes in the stable layers. A wave with a certain wavelength directly feels the lower damping rate at a higher numerical resolution. Since the wave excitation rate is larger due to the larger convective velocities, a mode reaches a significantly larger amplitude. This explains why the g-mode velocity amplitudes increase with resolution.

4.4. Detailed shape of the entropy plateau

The initially flat entropy profile on the plateau changes during a simulation. However, it does not show a simple monotonic decline as in a corresponding MLT model. Instead, it has a complex height and parameter dependence (see the panels in the lower half of Fig. 17).

All models show a sharp entropy peak in the heating zone at the bottom of the entropy plateau. The entropy declines with height, indicating a con-

vectively unstable region consistent with MLT. However, the entropy minimum is not located at the top of the plateau but somewhere in the middle, typically in the lower half. Above the minimum, the entropy rises and has, in most models, a smooth monotonic transition to the stable layers above the convection zone. An exception is the model lc0gh (with realistic heating rate and highest resolution, cf. the two bottom panels in the center column in Fig. 17): It shows a second minimum at the top of the plateau.

Note, that even if the entropy gradient is positive in some parts of the convection zone and therefore the stratification is formally stable there, the matter is heated in the shallow zone at the bottom and the plumes maintain their entropy excess and remain buoyant over the entire convection zone (indicated by the bright color of the plumes in e.g. Fig.8).

We interpret the entropy rise at the top of the plateau of most models as due to mixing of high-entropy material from the stable layers above into the convection zone. This mixing depends on the velocity amplitude, the numerical resolution, and time.

A significant part of the flow close to the upper boundary of the entropy plateau is due to wave motions. These are almost reversible and have a low mixing efficiency and cause a diffusion of entropy due to numerical viscosity. In addition ro numerical mixing there may be a finite amount of physical mixing.

While higher resolution means less dissipation it also means larger amplitude of the motions that cause the mixing. A large heating rate means strong mixing but also a quick rise of the plateau so that the relative effect remains small. The model lc0cg (which has the largest heating rate) has the largest absolute amount of mixing (the highest entropy rise at upper part of the plateau, see third panel in right column in Fig. 17). However, the relative effect is smaller than for the models with lower heating rate (fourth panel in right column in Fig. 17).

The resolution effect onto the models with large heating rate (left column in Fig. 17) is only moderate. The relatively quick rise of the entropy plateau value seems to limit the region with the entropy contamination from above. The dissipa-

tion of entropy is similar for all four tested resolutions.

In the models with realistic heating rate (center column in Fig. 17) the entropy profile changes qualitatively and quantitatively. The low-resolution models show a strong rise of entropy, whereas the highest resolution model has a well-defined minimum close to the top of the plateau. The effect of this minimum can be seen e.g. in Fig.8 or Fig.16 as tiny dark plumes emanating from the top unstable layers downward. An initial extra minimum in the entropy profile of model lc0gg (600x200 points) vanishes during the simulation. The minimum of model lc0gh (1200x400) remains during the available simulation time. The profile for very high resolutions and long simulation time is therefore not predictable, yet.

The change in the entropy profile due to this slow mixing has an impact on the flow for the runs with low resolution and low heating rate. While the flow patterns during the onset and early stages of convection are very similar when a proper scaling of the amplitudes of the fluctuations is taken into account (see Fig. 13) the patterns differ after a sufficiently long simulation time (see Figs. 20 and 21). The contamination of the convection zone with high-entropy material is so strong that the stratification is partly stabilized. The convective velocities in the top part of the entropy plateau decrease, and the typical cell sizes become noticeably smaller.

4.5. Modes

To further investigate the waves encountered in the simulations, we construct k-ω diagrams from Fourier analyses. An example is shown in Fig. 22 for an arbitrary height point inside the upper stable region for the run lc0gg.

In order to produce such a diagram, we collect all points for a single quantity (the vertical velocity) for a chosen height and all time steps of an interval into a 2D array. For the example from the lc0gg run, the array has a space axis with 600 points spanning 33 Mm, and a time axis with 12000 points spanning 6000 s. Next, a possible trend in time is removed by subtracting a parabola fitted to the time-dependent spatial average of the data. This is actually not necessary for the vertical velocities. But it is essential for

10

data like the entropy that has a large average value and a trend in time. To avoid signals due to the misfit of the beginning and end of the sequence, the data is faded in and out by multiplying with a cosine-bell function. A 2D Fourier analysis is applied and the power-spectrum is computed. The latter is smoothed in frequency space by applying a (1/4, 1/2, 1/4) filter. To emphasize small signals, the power$^{-0.1}$ is plotted in the examples.

A simple mode with a certain wavelength and period would give a single (dark) spot in a k-ω diagram. Imperfections (e.g. due to interaction with convection or damping) would cause a smearing in frequency. Plane-parallel modes are found on the ν axis. Static signals (e.g. processes on time-scales exceeding the interval) are located on the $1/\lambda$ axis.

While a horizontally moving sine wave would give a single spot, a more complex function that travels horizontally with a certain speed would produce an entire ray with a slope $\nu\lambda$. Mode families give rise to ridges. Their detailed shape depends on the background stratification. Convection does not consist of discrete modes. Instead, it has only typical time and length scales and gives a smeared blob.

On the left side of Fig. 22, pressure waves (p-modes) are visible, reaching up to the top of the diagram. In fact, a reflection of the pattern occurs at the top of the figure. The sampling rate is not quite high enough to fully resolve all p-modes, which leads to this aliasing phenomenon.

The bottom part of the diagram (below the Brunt-Väisälä-frequency of $0.1\,\mathrm{s}^{-1}$) is dominated by gravity waves (g-modes). At longer horizontal wavelengths (small $1/\lambda$) individual ridges are visible. The top ridge (highest frequency) corresponds to the mode with largest vertical wavelength. Modes with smaller wavelength have a lower frequency (contrary to the behavior of p-modes). The g-modes with very small horizontal or vertical wavelength are not resolved individually and only give a dark "band".

The inconspicuous convective signature is the inclined flattened streak in the very lower left corner at $\lambda{>}1\,\mathrm{Mm}$, $t{>}100\,\mathrm{s}$. To exhibit the location of the convective signal in the k-ω diagrams more clearly Fig. 23 shows only the lower left corner of the entire diagram, with a non-linear scale that magnifies the region corresponding to long time-

scales and large wavelength even further. The figure shows a sequence of k-ω diagrams for various heights inside the stable regions and the convection zone.

All plots show p-modes with varying relative power. Inside the convection zone (y=4.70 Mm) they are barely visible above the huge background of the convective motions. However, in the stable layers close to the top of the computational domain they have almost the same total power as the gravity waves. The top panels in Fig. 23 show a single ridge between p-modes and g-modes: the fundamental mode (f-mode).

The gravity waves in the lower cavity (four top panels) have a higher Brunt-Väisälä-frequency than the modes in the upper cavity. Both wave families can be traced into the convection zone (y=1.79 Mm and y=7.45 Mm).

The extended convective blob is visible in all panels, reaching from the convection zone, where it dominates the power, far into the stable regions. A k-ω diagram even closer to the top than the last panel in Fig. 23 does not show a clear signature of the convective velocities anymore (the location of the last panel was chosen accordingly).

While the convective flow overshoots into the stable regions, the stable regions "shoot back", they tunnel somewhat into the region with the essentially flat entropy profile. This overlap of flows leads to the mixing of high-entropy material into the convection zone, as described in Sect. 4.3. The region where convective flows and gravity waves can interact is vertically extended and not confined just to the top layer of the convection zone. During the onset phase of convection, gravity waves are excited in the upper stable region well before the convective upflows reach the upper boundary of the entropy plateau. Convective elements (plumes) do not just "smash" against the boundary. Instead, the braking of the flow (and the excitation of the waves) occurs over some extended region. Rising co-moving fluid packets (adiabatically) compress the material between themselves and the top boundary. The pressure rises, brakes the vertical movement of the convective element, and accelerates material horizontally. As a result, the vertical motion of the convective element is turned into a horizontal flow and the over-pressure at the top lifts the boundary of the entropy plateau slightly. The material in the sta-

ble region is pushed away both horizontally and vertically. The reaction of the stable layers has an oscillatory component – the g-modes. However, as long as the local over-pressure from the convection zone below exists, some distortion remains in the stable layers. The distortion closely follows the time-evolution of the convective flow and has the same signature in a k-ω diagram.

While the picture as described above remains qualitatively the same for all resolutions and heating rates in our grid, there are some differences and trends visible. The position of a mode peak in a k-ω diagram remains essentially the same for all runs since it only depends on the background stratification which only changes slightly towards the end of the lc0cg run (largest heating rate). However, more heating means higher convective velocities and smaller time scales. Therefore, the relation between time-scales of convection and modes changes. The convective blob moves closer to the ridges of the g-modes, and a separation becomes more difficult.

The mode peaks appear sharper at lower heating rates, where less interaction with convection and less change in the background stratification lead to longer mode lifetimes and "cleaner" peaks. Convective scales are slightly smaller at lower heating rates, indicated by a shifted maximum and stronger tail towards higher frequencies.

An increase in resolution does not change the frequencies of already visible modes noticeably. However, more and more ridges appear and this indicates that the wide and flat g-mode nodes are not well enough resolved.

4.6. Mixing

Our mixing analysis is preliminary. Mixing inside the convective region is directly correlated with the averaged vertical velocities (top panels Fig. 17). An important feature of these velocity profiles is the substantial decline of the velocities within the convective region, starting at a position several hundred km above the bottom and below the top of the convection layer. These plots indicate that the decay of the vertical velocity field is exponential. Outside the convective region, the velocity amplitudes of the g-modes dominate the averaged vertical velocity profile. Due to the wave nature of g-mode oscillations, these rather large velocities correspond to mixing that is orders of magnitude less efficient than that inside the convection zone, and possibly negligible far away from the convection zone. The fact that the g-mode velocity amplitudes superimpose onto the decay of the convective velocity field complicates deriving the effective mixing in and into the stable layers. A preliminary analysis of the oscillation modes (Sect. 4.5) suggests that the convective velocity field and therefor the corresponding mixing continues the exponential decay into the stable layer. However, future analysis has to reveal the extent of the overshooting plumes interact with the horizontal motions of the g-modes, potentially leading to increased mixing in the stable layers beyond the convective boundary.

We have performed two test runs with enhanced heating rate and low to moderate resolution (lc2df and lc2dg, Fig. 5) and with three individual fluids in the three different layers of the setup. The fluids are treated separately by the code but have the same properties, i.e. the same molecular weight. We use these fluids as passive tracer particles to establish an approximate upper limit on mixing (Hurlburt et al. 1994). We find that there is a finite mixing of material across both boundaries. In both runs at both boundaries there are typically four horizontal layers involved in the main abundance transition. Mixing from the top stable layer into the convection zone seems to be more efficient for the higher resolution run. The top layer abundance reaches a mass fraction of approximately 10^{-5} inside the convection zone, whereas the lower resolved simulation (lc2df) reaches a few 10^{-6}. Mixing of material into the convection zone from below is at a similar level but shows a significant upward trend at late times (after several convective turn-over times). Mixing of material from below the convection zone is roughly at the same level as mixing from above, but more efficient for the lower resolution case than for the higher resolution case.

Mixing at the top unstable-stable interface can be seen in the model lc0dh with large heating rate and high resolution (cf. the bottom panel in Fig. 18). The shear flows at the top of the convection zone "peel off" high-entropy material from the stable layers above. This material keeps its identity for some time, remains hotter than the surroundings, and is visible as bright spots in the

center of some vortices. The rather long survival time of these vortices may be a 2D artifact.

The material in the lower stable zone is too dense to be mixed directly into the convection zone. However, the entropy (and density) jump is smoothed out over time. Then the flow at the bottom of some plumes becomes strong enough to lift up slightly cooler material from below that is finally mixed into the convection zone. It is visible as the dark areas directly beneath the plumes in Fig. 18.

To some degree models with large heating rate and low resolution seem to have similar properties as models with smaller heating rate and higher resolution. We will therefore continue to perform simulations with too large heating rates in addition to the runs with more realistic parameters.

5. Discussion and conclusions

We presented the first set of hydrodynamic simulations specifically addressing the conditions in the convection zone close the peak luminosity of the He-shell flash. Compared to previous calculations of other stellar convection zones our simulations reveal some important differences. One of the most important is the stiffness of the convective boundaries of He-shell flash convection in contrast to the shallow surface convection of A-stars and white dwarfs as studied by Freytag et al. (1996). Other examples include solar-type convection (Dintrans et al. 2005) or much of the parameter range in relative stability between the unstable and stable layers studied by Rogers & Glatzmaier (2005). Even in the simulations of core convection in A-type stars (Browning et al. 2004) convective plumes can cross the convective boundary significantly. In shallow surface convection zones the convective downdrafts easily cross the convection boundary and penetrate deep into the stable layers beneath. No significant g-mode excitation has been detected by Freytag et al. (1996), which is probably due to the absence of a stiff resonance floor with which convective plumes and the pressure field interact. However, it seems that because of this particular feature of the shallow surface convection zone Freytag et al. (1996) were able to study the decay of the convective velocity field in isolation. In our He-shell flash convection we do see exponential decay of the convective veloc-

ity field as well. However it already starts inside the convection zone, and at or beyond the border quickly intermingles with the effects of the gravity waves.

The comparison to the new O-shell convection simulations by Maekin & Arnett (2006, and 2006b, in prep) confirms the importance of g-modes for mixing and to correctly account for the physics at the convective boundary. Similar to our simulations their convective boundaries are very stiff, with overshooting of convective plumes into the stable layer reduced to a minimum. More important are horizontal wave motions which eventually induce turbulent mixing. A partial mixing zone at the convective boundaries is minimal. The O-shell convection simulations include μ-gradients, contrary to our similations. μ gradients increase the impenetrable character of the convective boundaries significantly, and we plan to include this effect in our simulations in the future.

We tentatively compare the mixing length convective velocity profile from our 1D stellar evolution template model with the averaged vertical velocities in the hydrodynamic simulation with realistic heating rate in Fig. 24. Obviously, there are many differences in the assumptions of the two calculations, including geometry, micro-physics and of course the treatment of convection itself. Nevertheless, we find that the absolute value of the velocities inside the convection zone are similar. We do observe a different profile in the two representations. The hydrodynamic simulation show a more pronounced slope in the velocity profile within the convection zone than the MLT profile. The peak in the velocity profile from the hydrodynamic simulation is close to the bottom of the convection zone. The most important difference is the significant decline of the velocity field already inside the convection zone. Near the lower boundary the vertical velocity is almost 3 orders of magnitude lower than the peak value. This may have implications for s-process nucleosynthesis as nuclei are on average exposed much longer to the hottest temperature at the very bottom of the convection zone. This should be considered in particular for cases that involve branchings sensitive to the convective time-scale of He-shell flash convection, like ^{128}Xe (Reifarth et al. 2004).

Consistent with previous work on stellar interior convection we observe a rich spectrum of g-

modes excited in the stable layers. These g-modes interact with the decaying convective flows at the boundary of the unstable region. Our simulations show that He-shell flash convection displays the main ingredients observed in previous stellar convection simulations, but with different relative contributions of the various components. The actual overshooting of convective plumes across the convective boundaries is much smaller than in shallow surface convection and O-shell convection, while the excitation of internal gravity is probably stronger because the boundaries are stiffer. Although there is a significant overlap of the two processes we have shown that the analysis of the oscillation modes by means of the k-ω diagram allows us to disentangle the different contributions to the velocities. With this approach we observe that there is a finite mixing of convective motions accross the convective boundary. We postpone quantifying this mixing to future work. In addition, we plan to quantify the contribution from wave mixing at He-shell flash convection boundaries.

We have identified a number of numerical problems at low heating rates and low resolution that need to be dealt with in future 3D runs. These include the diffusion of entropy from above into the top zones of the unstable layer, impeding the development of the correct hydrodynamic flow-pattern. Our convergence and heating rate study shows that simulations with larger heating rate are in some ways equivalent to runs with higher resolution. Properties like the exponential decay rate of the convective velocity field seem to be only weakly dependent on the heating rate. However, the excitation of g-modes and their amplitudes depends sensitively on both the resolution and the heating rate. While we do see signs of convergence for the convective properties of our simulations, this is not the case for the g-modes.

We consider 2D vs. 3D systematics, the effect of μ-gradients, a realistic treatment of nuclear energy generation, and a more detailed study of the interaction of wave mixing with convective overshooting as our most immediate tasks for future improvements. In addition we can make our simulations more realistic by adopting an apppropriate stellar equations of state, by accounting for the spherical geometry of the He-shell, and by including a realistic gravitational potential.

REFERENCES

Alexander, D. & Ferguson, J. 1994, ApJ, 437, 879

Althaus, L. G., Serenelli, A. M., Panei, J. A., Córsico, A. H., García-Berro, E., & Scóccola, C. G. 2005, A&A, 435, 631

Angulo, C., Arnould, M., & Rayet, M. et al. 1999, Nucl. Phys., A 656, 3, NACRE compilation

Arlandini, C., Käppeler, F., Wisshak, K., Gallino, R., Lugaro, M., Busso, M., & Straniero, O. 1999, ApJ, 525, 886

Asida, S. M. & Arnett, D. 2000, ApJ, 545, 435

Baltrusaitis, R., Gittings, M., Weaver, R., Benjamin, R., & Budzinski, J. 1996, Phys. Fluids, 8, 2471

Bazan, G. & Arnett, D. 1998, ApJ, 496, 316

Beers, T. C. & Christlieb, N. 2005, ARAA, 43, xxx

Belle, K., Coker, R., & Hueckstaedt, R. 2005, ApJ

Blöcker, T. 1995, A&A, 297, 727

Böhm-Vitense, E. 1958, Z. Astrophys., 46, 108

Browning, M. K., Brun, A. S., & Toomre, J. 2004, ApJ, 601, 512

Brun, A. S. 2004, Solar Phys., 220, 333

Busso, M., Gallino, R., & Wasserburg, G. J. 1999, ARA&A, 37, 239

Cristallo, S., Gallino, R., & Straniero, O. 2004, Memorie della Societa Astronomica Italiana, 75, 174

Dendy, E. & Gittings, M. 2005, Los Alamos report LA-UR-05-1642

Denissenkov, P. A. & Herwig, F. 2003, ApJ Lett., 590, L99

Dintrans, B., Brandenburg, A., Nordlund, Å., & Stein, R. F. 2005, A&A, 438, 365

Freytag, B., Ludwig, H.-G., & Steffen, M. 1996, A&A, 313, 497

Freytag, B., Steffen, M., & Dorch, B. 2002, Astr. Nachr., 323, 213

Geisler, D., Smith, V. V., Wallerstein, G., Gonzalez, G., & Charbonnel, C. 2005, AJ, 129, 1428

Herwig, F. 2000, A&A, 360, 952

—. 2004, ApJ, 605, 425

Herwig, F. 2004, ApJS, 155, 651

Herwig, F. & Austin, S. M. 2004, ApJ Lett., 613, L73

Herwig, F., Blöcker, T., Schönberner, D., & El Eid, M. F. 1997, A&A, 324, L81

Holmes, R., Dimonte, G., Fryxell, B., Gittings, M., Grove, J., Schneider, M., Sharp, D., Velikovich, A., Weaver, R., & Zhang, Q. 1999, J. Fluid Mech., 389, 55

Hueckstaedt, R., Batha, S., Balkey, M., Delamater, N., Fincke, J., Holmes, R., Lanier, N., Magelssen, G., Scott, J., Taccetti, J., Horsfield, C., Parker, K., & Rothman, S. 2005, Ap&SS, 298, 255

Hurlburt, N. E., Toomre, J., & Massaguer, J. M. 1984, ApJ, 282, 557

Hurlburt, N. E., Toomre, J., & Massaguer, J. M. 1986, ApJ, 311, 563

Hurlburt, N. E., Toomre, J., Massaguer, J. M., & Zahn, J.-P. 1994, ApJ, 421, 245

Iben, Jr., I. & Renzini, A. 1983, ARA&A, 21, 271

Iglesias, C. A. & Rogers, F. J. 1996, ApJ, 464, 943

Langer, N., El Eid, M., & Fricke, K. J. 1985, A&A, 145, 179

Lugaro, M., Davis, A. M., Gallino, R., Pellin, M. J., Straniero, O., & Käppeler, F. 2003a, ApJ, 593, 486

Lugaro, M., Herwig, F., Lattanzio, J. C., Gallino, R., & Straniero, O. 2003b, ApJ, 586, 1305

Maekin, C. & Arnett, D. 2006, ApJ Lett., in press

Mazzitelli, I., D'Antona, F., & Ventura, P. 1999, A&A, 348, 846

Merryfield, W. J. 1995, ApJ, 444, 318

Nordlund, A. 1982, A&A, 107, 1

Nordlund, A., Spruit, H. C., Ludwig, H.-G., & Trampedach, R. 1997, A&A, 328, 229

Porter, D. H. & Woodward, P. R. 1994, ApJS, 93, 309

—. 2000, ApJS, 127, 159

Reifarth, R., Alpizar-Vicente, A., Hatarik, R., Bredeweg, T. A., Esch, E.-I., Greife, U., Haight, R. C., Kronenberg, A., O'Donnell, J. M., Rundberg, R. S., Schwantes, J. M., Ullmann, J. L., Vieira, D. J., & Wouters, J. M. 2005, in ASP Conf. Proc. 769, 1323–1326

Reifarth, R., Käppeler, F., Voss, F., Wisshak, K., Gallino, R., Pignatari, M., & Straniero, O. 2004, ApJ, 614, 363

Renda, A., Fenner, Y., Gibson, B. K., Karakas, A. I., Lattanzio, J. C., Campbell, S., Chieffi, A., Cunha, K., & Smith, V. V. 2004, MNRAS, 354, 575

Robinson, F. J., Demarque, P., Li, L. H., Sofia, S., Kim, Y.-C., Chan, K. L., & Guenther, D. B. 2004, MNRAS, 347, 1208

Rogers, T. M. & Glatzmaier, G. A. 2005, ApJ, 620, 432

Siess, L., Livio, M., & Lattanzio, J. 2002, ApJ, 570, 329

Stein, R. F. & Nordlund, A. 1989, ApJ Lett., 342, L95

Stein, R. F. & Nordlund, A. 1998, ApJ, 499, 914

Travaglio, C., Gallino, R., Arnone, E., Cowan, J., Jordan, F., & Sneden, C. 2004, ApJ, 601, 864

Venn, K. A., Irwin, M., Shetrone, M. D., Tout, C. A., Hill, V., & Tolstoy, E. 2004, AJ, 128, 1177

Ventura, P., D'Antona, F., & Mazzitelli, I. 2000, A&A, 363, 605

—. 2002, A&A, 393, 215

Young, P. A. & Arnett, D. 2005, ApJ, 618, 908

Young, P. A., Meakin, C., Arnett, D., & Fryer, C. L. 2005, ApJ Lett., 629, L101

Zinner, E. 1998, Ann. Rev. Earth Planet. Sci., 26, 147

TABLE 1

PROPERTIES OF HE-SHELL REGION IN STELLAR MODEL 70238

	box bot.	conv. bot.	conv. top	box top
D/(cgs)	0.000E+00	1.634E+12	1.051E+12	0.000E+00
R/R$_\odot$	1.088E-02	1.324E-02	2.206E-02	2.681E-02
H$_p$/R$_\odot$	1.296E-03	2.439E-03	1.258E-03	2.337E-03
M$_r$/M$_\odot$	0.5230	0.5704	0.5918	0.5929
ρ/(cgs)	1.267E+05	1.173E+04	7.004E+02	2.782E+01
T/K	1.544E+08	2.479E+08	4.631E+07	4.872E+07
ln P(cgs)	48.68	46.62	42.16	39.16
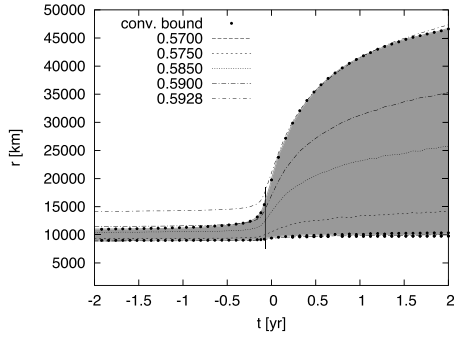
Fig. 1.— Time evolution of the radial location of the He-shell flash convection zone based on the 1D stellar evolution model. Time is set to zero at the peak of the He-burning luminosity. The ordinate is zero at the stellar center. The grey shaded area represents the He-shell flash convection zone. Dots along the boundary indicate individual time steps in the 1D evolution model sequence. The vertical solid line at $t = -0.07$ yr indicates the position and extent of the hydrodynamic simulation box. Dashed and dotted lines correpsond to the Lagrangian coordinates given in the legend, and visualize the expansion of the He-shell as a result of the He-shell flash.
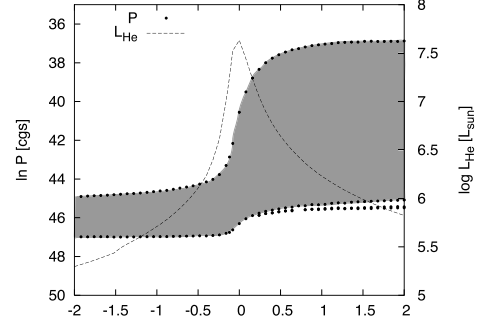
Fig. 2.— Time evolution of the He-burning luminosity and the pressure at the boundary of the convection zone for the He-shell flash. The time axis, grey shades, and dots have the same meaning as in Fig. 1.
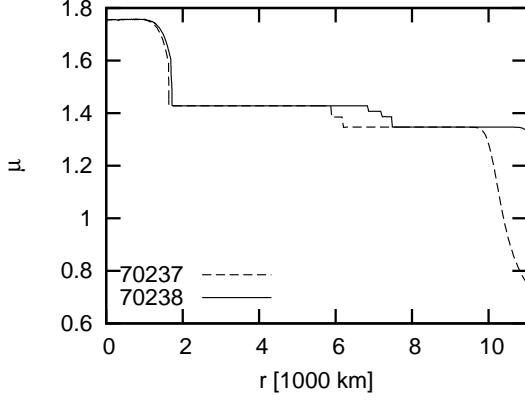
Fig. 3.— Mean molecular weight of the fully ionized material in the simulated shell of the two stellar evolution models before the peak He-burning flash luminosity. The radius is set to zero at the stellar radius of 7500km, coinciding with the bottom of the box for the hydrodynamic simulations. The two steps in the mean molecular weight are associated with the bottom of the He-shell flash convection zone at 1650km and the top at 7732km in model 70238. For model 70237 (dashed line) the bottom of the H-rich envelope is located at $r = 10000$km.

		e 210x70	f 300x100	g 600x200	h 1200x400	I 2400x800
c	100			10000		
d	30	10000	10000	10000	4600	900
e	10			10000		
f	3			10000		
g	1	10000	15000	16500	4300	
h	1./3.		10000	16500		
I	1./10.		10000	20000		

Fig. 5.— The grid in resolution and heating rate of the standard 2D simulation set lc0. In the figure captions the combination of two letters identifies the simulation in this grid. The first letter gives the heating rate, the second the resolution. For example, run df has a heating rate of 30 times the standard case and a 300x100 grid. The numbers in the table give the length of the run in seconds. The standard heating rate g corresponds to what is described in Sect. 3.2.

Fig. 4.— The velocity profiles from two subsequent models of the 1D stellar evolution model track using the mixing-length theory. Our hydrodynamic simulations resemble the conditions of model 70238.
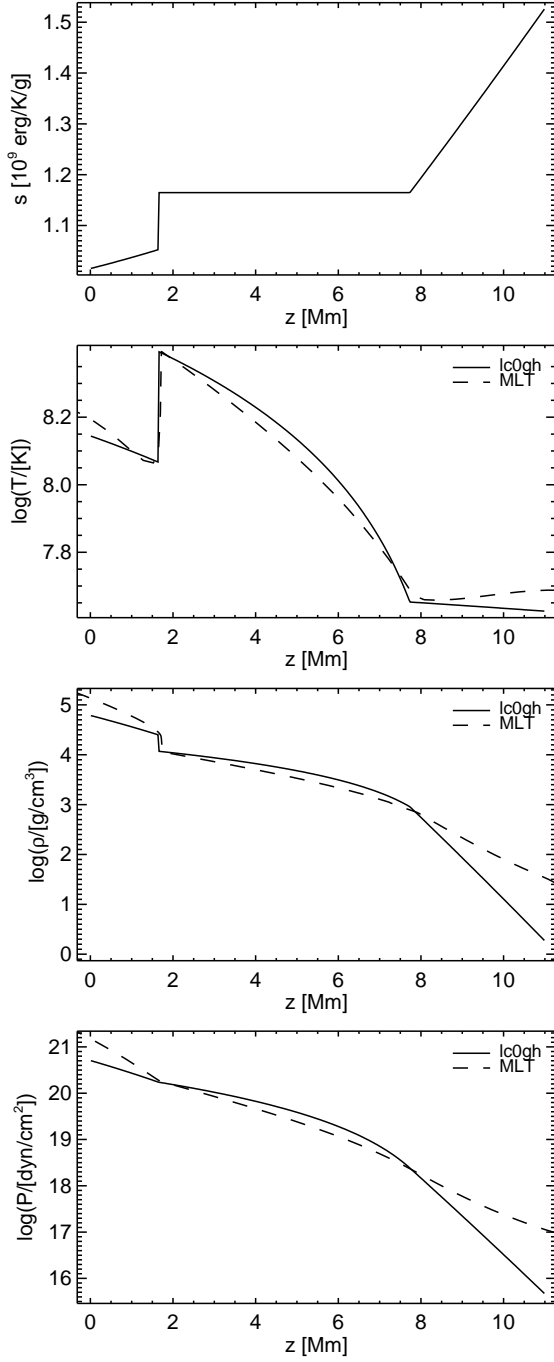
Fig. 6.— The initial entropy, temperature, density, and pressure stratifications of the hydrodynamic simulations (solid line) and the temperature, density and pressure from the 1D model ET2/70238 (dashed line).
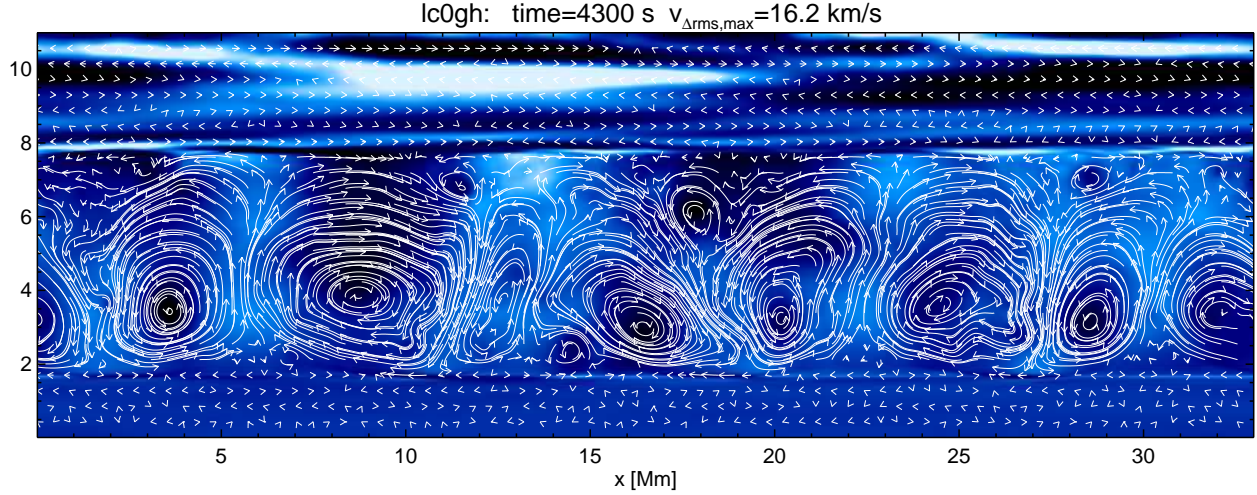
20

lc0gh: time=4300 s $v_{\Delta rms,max}$=16.2 km/s

Fig. 7.— Fully developed convection in a high-resolution 2D run with standard heating rate. The flow field is represented by 25x75 pseudo-streamlines, integrated over 100 s for the constant velocity field of this single snapshot of evolved convection during the lc0gh run. The color indicates the corresponding pressure inhomogeneities. The pressure itself does not deviate much from the initial values. Therefore, to make the fluctuations visible, the *horizontal average* of the pressure has been subtracted from the pressure value of every grid point. Bright means over-pressure (prominently where a "mushroom" approaches the upper boundary of the unstable region: compare with Fig. 8). Dark color indicates low-pressure (in the "eyes" of the vortices). The boundaries of the unstable layer (the entropy plateau in Fig. 6) at $y=1.7$ Mm and $y=7.7$ Mm are clearly marked in the flow field and the pressure inhomogeneities.

lc0gh: time=4300 s $v_{\Delta rms,max}$=16.2 km/s
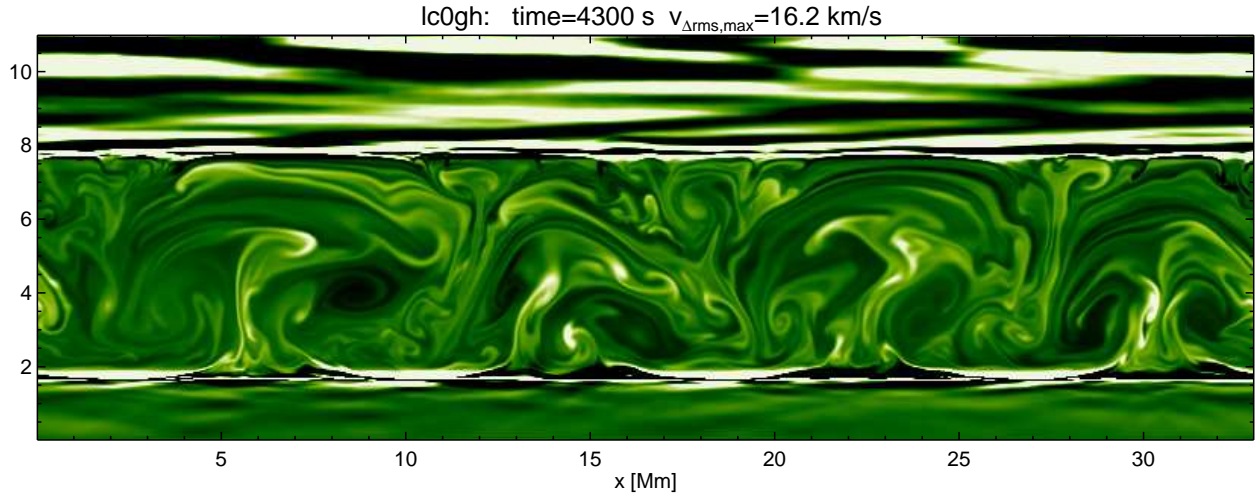
Fig. 8.— Entropy inhomogeneities for the same model of the lc0gh sequence as in Fig. 7. Again, the horizontal average of the entropy has been subtracted to render the small fluctuations visible. A bright color indicates material with higher entropy (and in fact higher temperature – due to the near pressure-equilibrium). Dark means low entropy (or temperature). The boundaries of the entropy plateau at $y=1.7$ Mm and $y=7.7$ Mm are again clearly visible in the change of the patterns. The subtraction of the horizontal mean causes bright features to be accompanied by dark horizontal stripes. These are pure artifacts of the visualization procedure and do not exist in the simulation data itself.
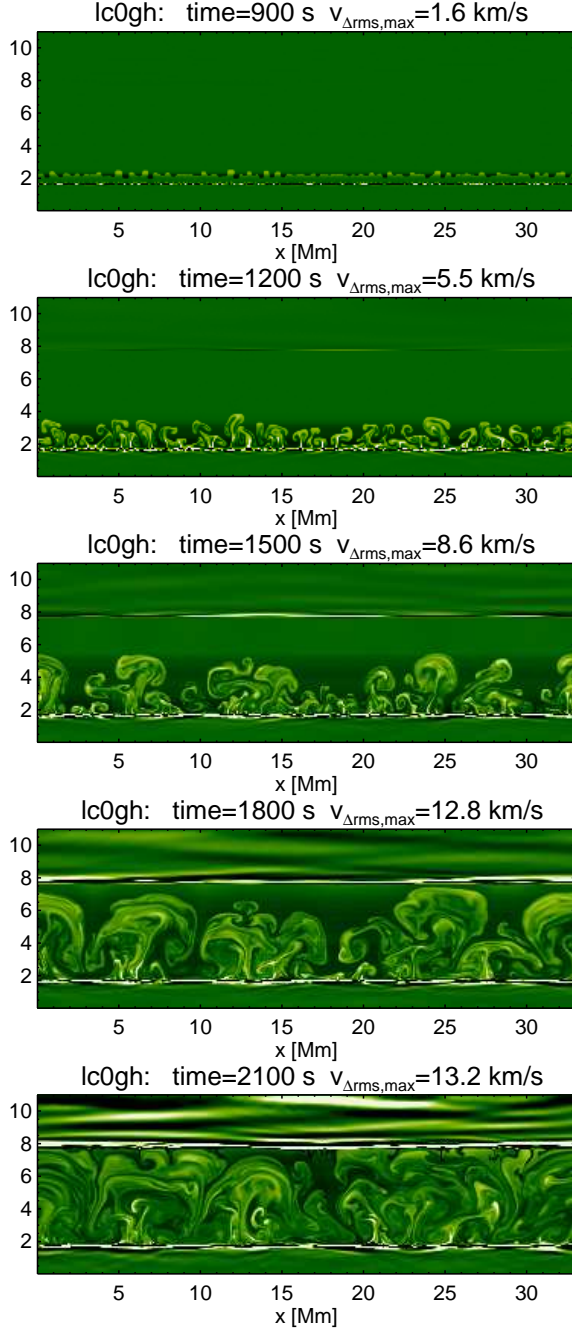
21

Fig. 9.— Entropy inhomogeneities during the onset of convection for the lc0gh run.
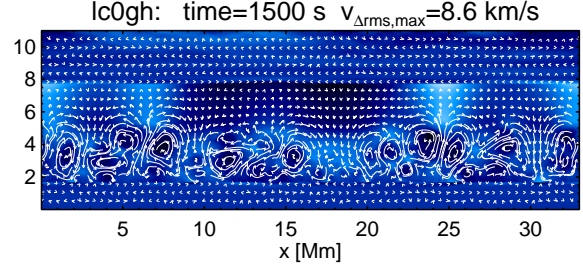

Fig. 10.— Like Fig. 7 for an earlier time during the onset of convection. Note the build-up of higher pressure regions above rising plumes that can be associated with the excitation of gravity waves in the top stable layer.
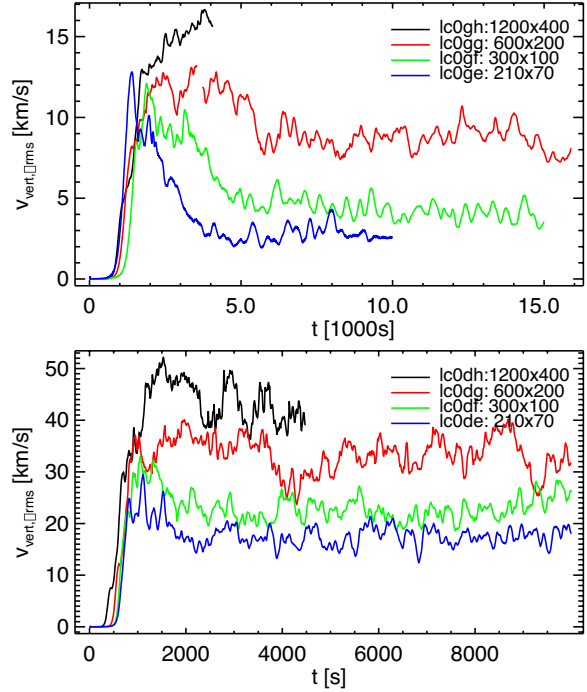

Fig. 11.— Time evolution of the maximum vertical, rms-averaged velocity for the standard heating rate g (top panel) and the enhanced heating rage d (bottom panel) for a range of resolutions.
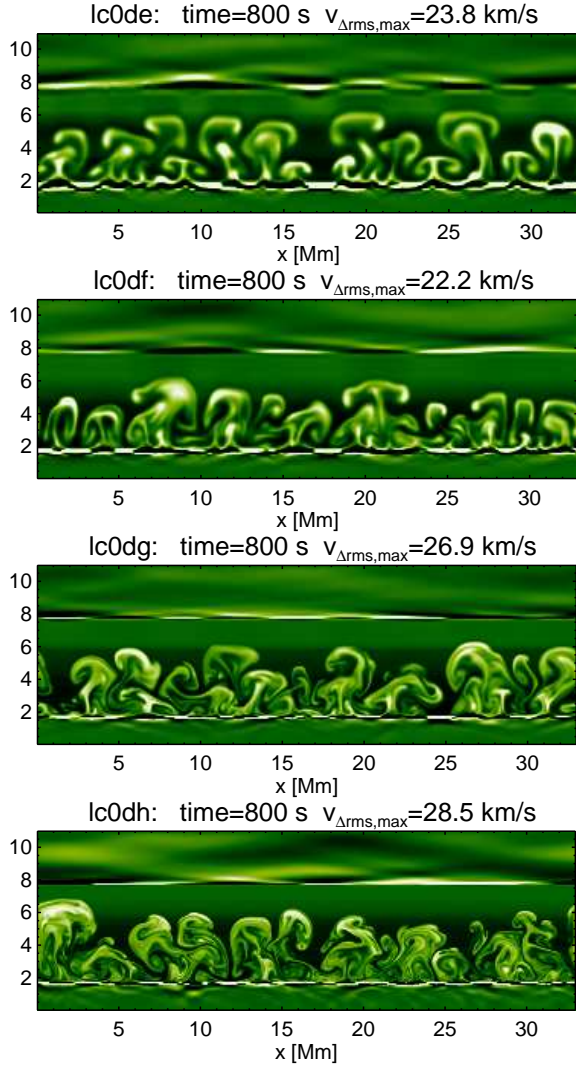
lc0de: time=800 s $v_{\Delta rms,max}$=23.8 km/s

lc0df: time=800 s $v_{\Delta rms,max}$=22.2 km/s

lc0dg: time=800 s $v_{\Delta rms,max}$=26.9 km/s

lc0dh: time=800 s $v_{\Delta rms,max}$=28.5 km/s

Fig. 12.— Resolution sequence of entropy inhomogeneities during the onset of convection.

lc0cg: time=608 s $v_{\Delta rms,max}$=20.9 km/s

lc0dg: time=783 s $v_{\Delta rms,max}$=24.6 km/s

lc0eg: time=986 s $v_{\Delta rms,max}$=21.5 km/s

lc0fg: time=1270 s $v_{\Delta rms,max}$=14.2 km/s

lc0gg: time=1600 s $v_{\Delta rms,max}$=9.1 km/s

lc0hg: time=2015 s $v_{\Delta rms,max}$=5.9 km/s
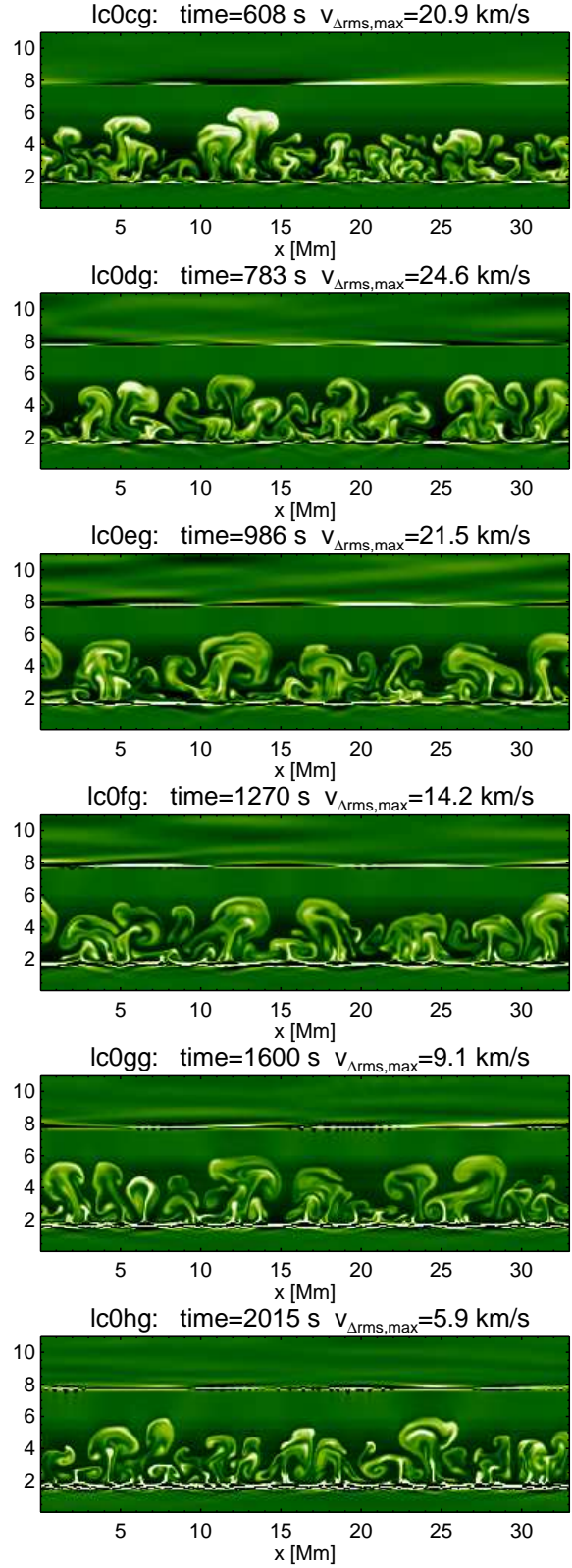
Fig. 13.— Heating rate sequence (decreasing from top to bottom) of entropy inhomogeneities during the onset of convection. The time steps are scaled with $q_{c}^{-0.21}$. The color palettes are scaled with $q_{c}^{0.5}$.
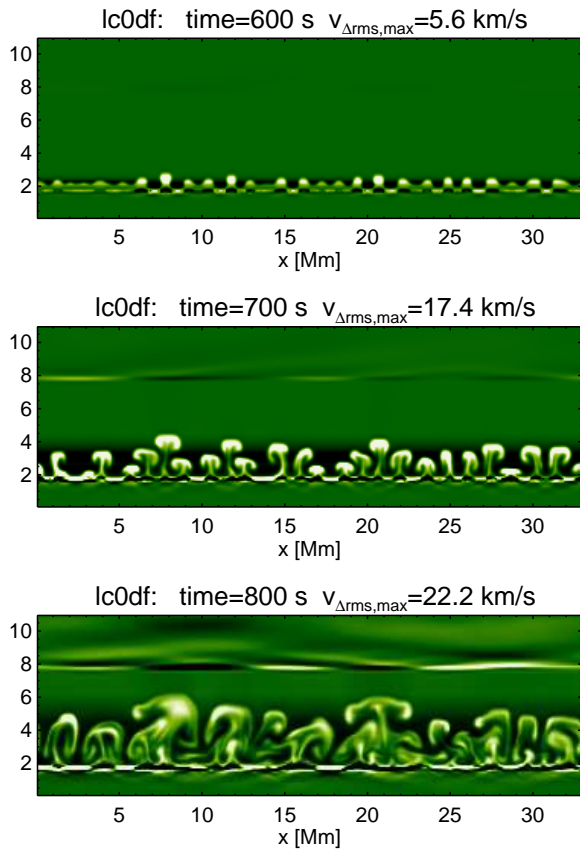
Fig. 14.— 2D lc0df run sequence of entropy inhomogeneities during the onset of convection. The same snapshot times and scaling is used as in Fig. 15.
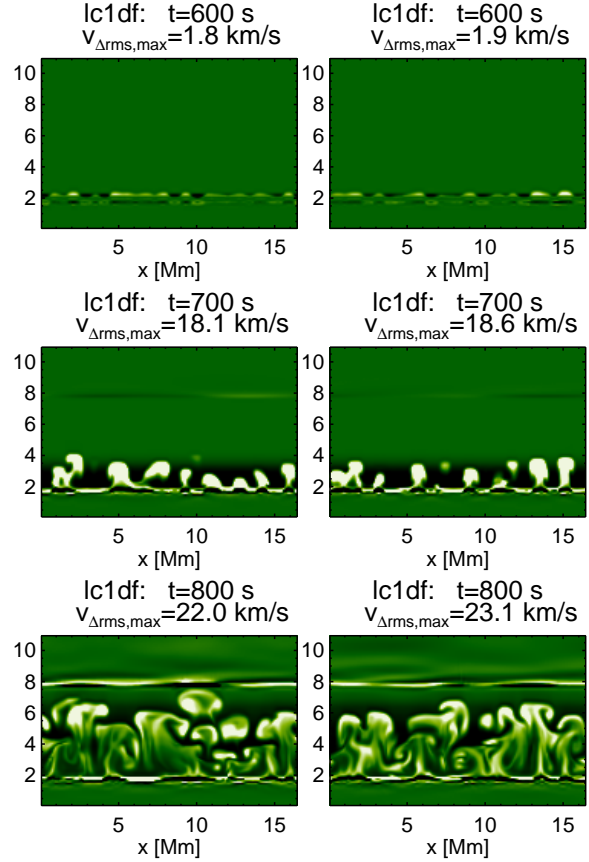
Fig. 15.— 3D lc1df run sequence of the entropy inhomogeneities during the onset of convection. The same snapshot times and scaling is used as in Fig. 14.
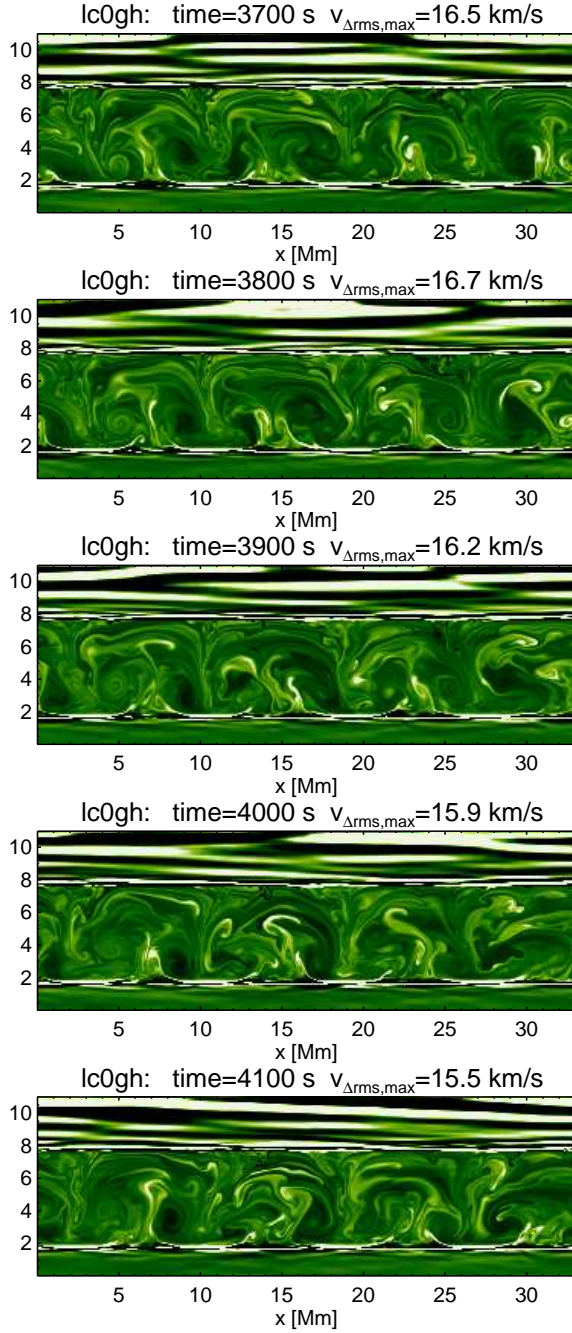
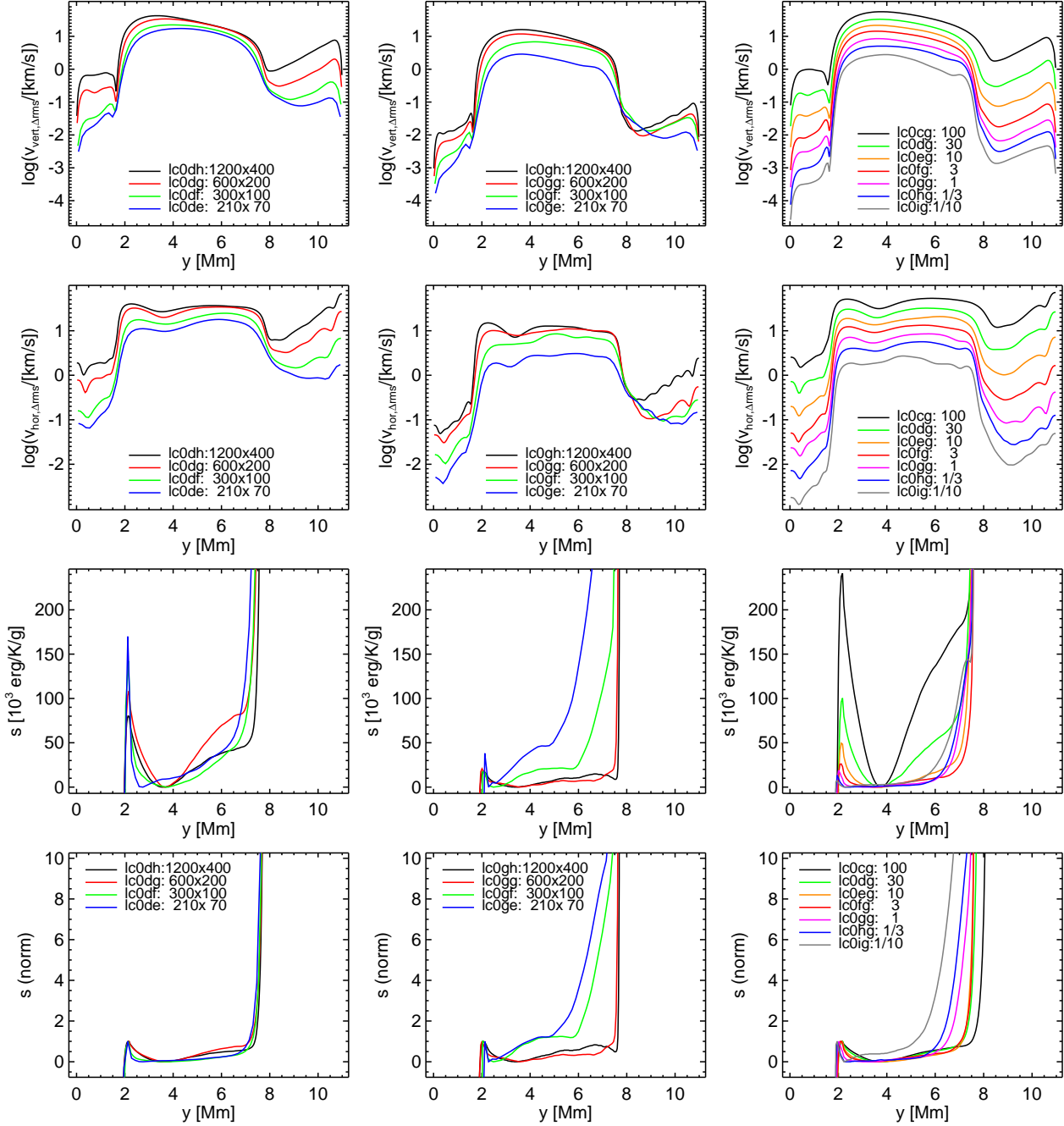Fig. 16.— Time-sequence of the entropy fluctuations for evolved convection, lc0gh run.

Fig. 17.— Some time-averaged quantities for various model sequences. Each column of panels refers to the same sequence. All panels in one row show the same quantity. Left column: runs with different resolutions and large heating rate (lc0dX). The averages are performed over the interval 1500-4500 s. Center column: runs different resolutions and realistic heating rate (lc0gX). The averages are performed over the (short) interval 3750-4300 s. Right column: runs with intermediate resolution (600x200) and different heating rates (lc0Xg). The averages are performed over the last 5000 s of each sequence. Top row: rms-fluctuations of the vertical velocity. Second row: rms-fluctuations of the horizontal velocity. Third row: mean entropy s shifted so that the minimum entropy on the plateau becomes zero. Bottom row: mean entropy s shifted as above and scaled to set the amplitude of the lower entropy bump to unity.
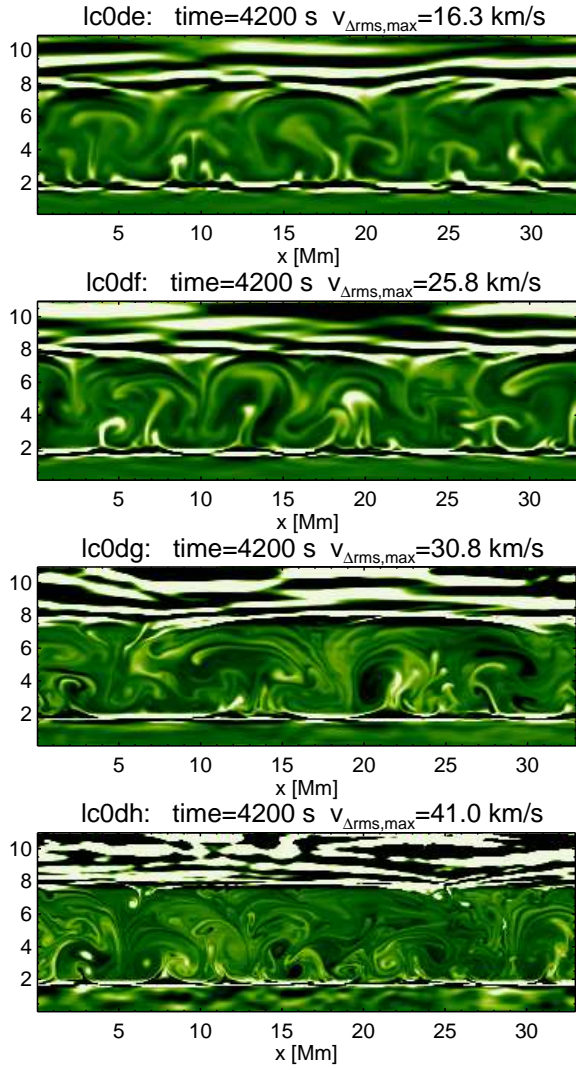
26

lc0de: time=4200 s $v_{\Delta rms,max}$=16.3 km/s

lc0ge: time=4200 s $v_{\Delta rms,max}$=3.0 km/s

lc0df: time=4200 s $v_{\Delta rms,max}$=25.8 km/s

lc0gf: time=4200 s $v_{\Delta rms,max}$=6.3 km/s

lc0dg: time=4200 s $v_{\Delta rms,max}$=30.8 km/s

lc0gg: time=4200 s $v_{\Delta rms,max}$=12.6 km/s

lc0dh: time=4200 s $v_{\Delta rms,max}$=41.0 km/s

lc0gh: time=4200 s $v_{\Delta rms,max}$=16.2 km/s

Fig. 18.— Resolution sequence and large heating rate, entropy inhomogeneities for evolved convection.
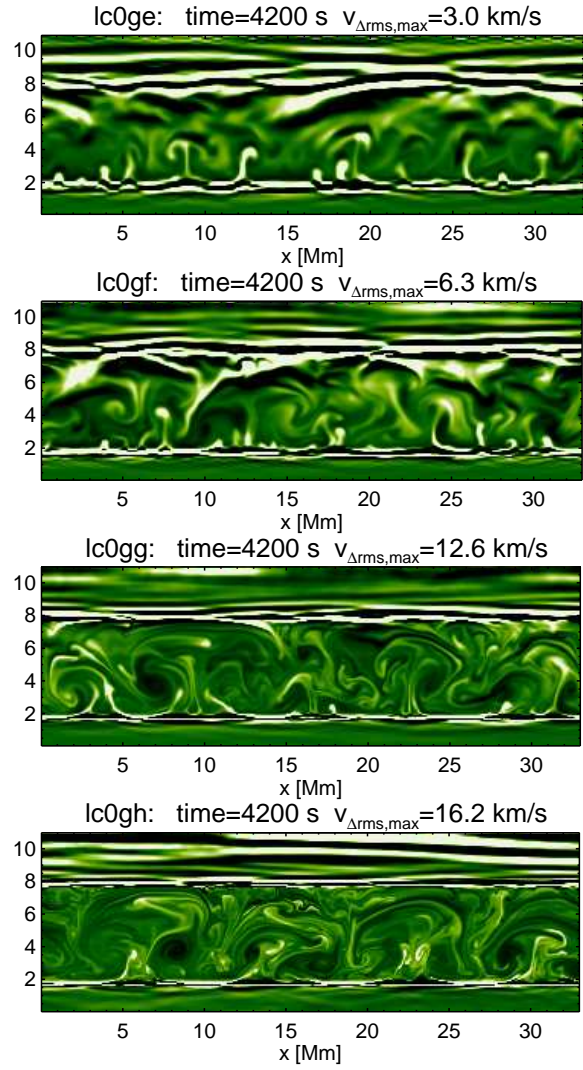
Fig. 19.— Resolution sequence and realistic heating rate, entropy inhomogeneities for evolved convection.
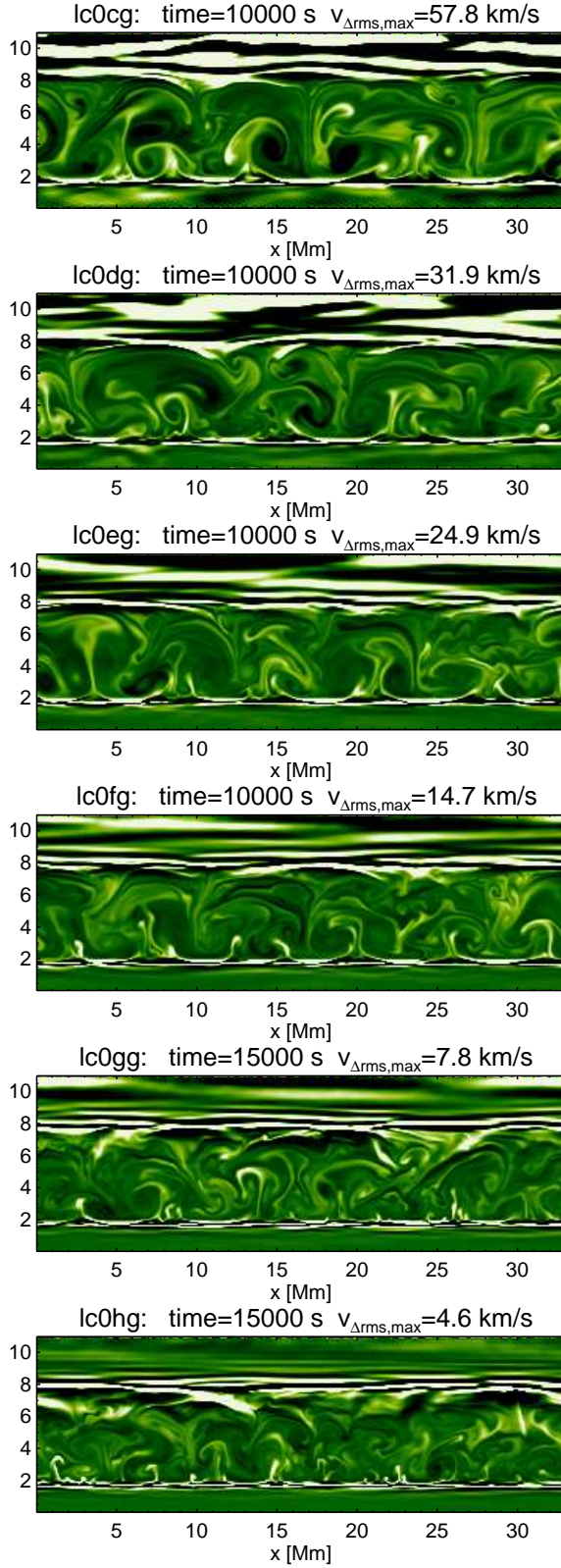
Fig. 20.— Heating rate sequence of the entropy inhomogeneities for evolved convection. The colors are scaled with $q_c^{0.5}$.
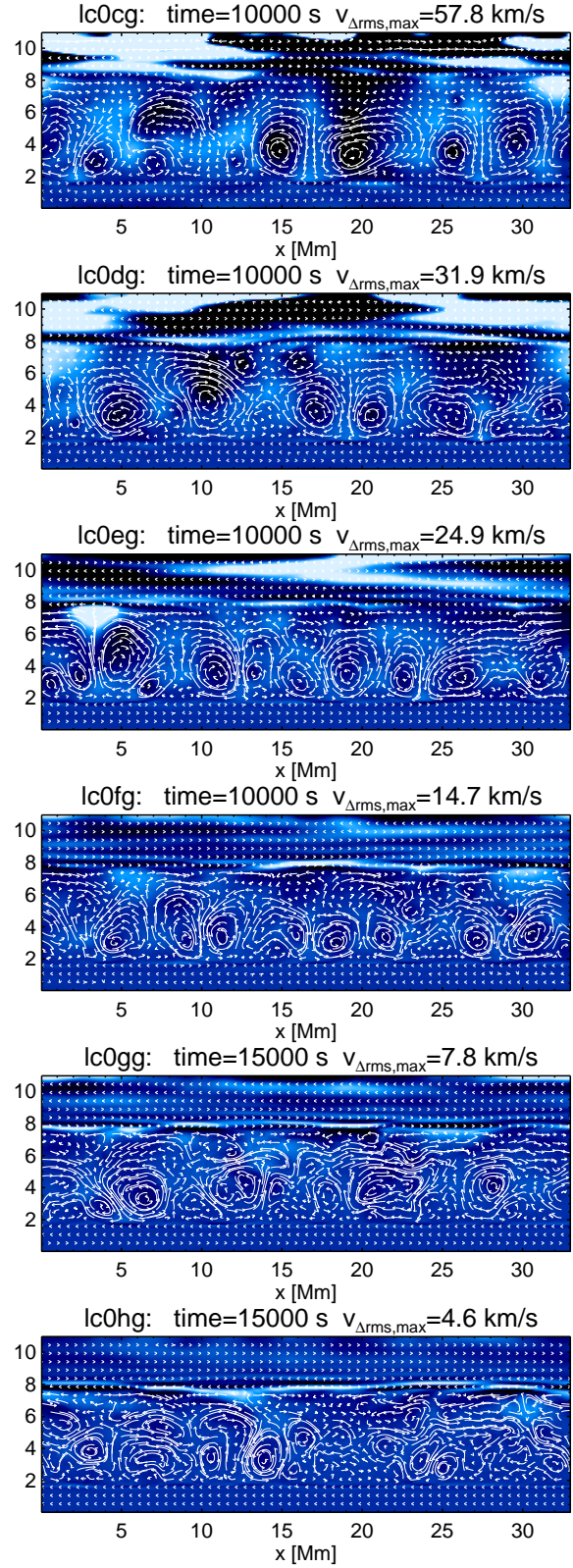
Fig. 21.— Pressure inhomogeneities and pseudo-streamlines for evolved convection for runs with different heating rates. The colors are scaled with $q_c^{0.5}$, the integration time for the pseudo-streamlines with $q_c^{0.5}$.
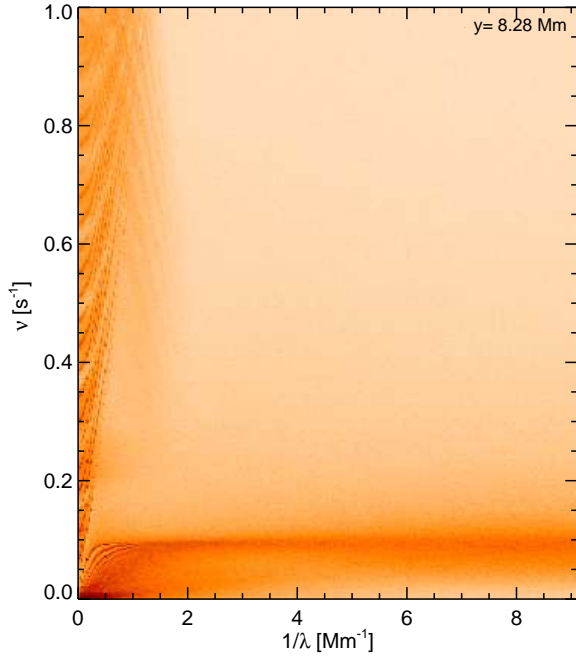
28

Fig. 22.— k-ω diagram (actually $1/\lambda$-ν diagram) for an arbitrary height in the upper stable region for run lc0gg. Both axes are linear and extend to the respective Nyquist frequencies. They are given by the sampling rate in time, $\nu_{t,\mathrm{Nyquist}}{=}1/2\Delta t_{\mathrm{sampling}}{=}1\,\mathrm{s}^{-1}$ and the horizontal grid size, $\nu_{x,\mathrm{Nyquist}}{=}1/2\Delta x_{\mathrm{grid}}{=}9.09\,\mathrm{Mm}^{-1}$. The signal strength goes from bright (low amplitude) to dark (high amplitude).
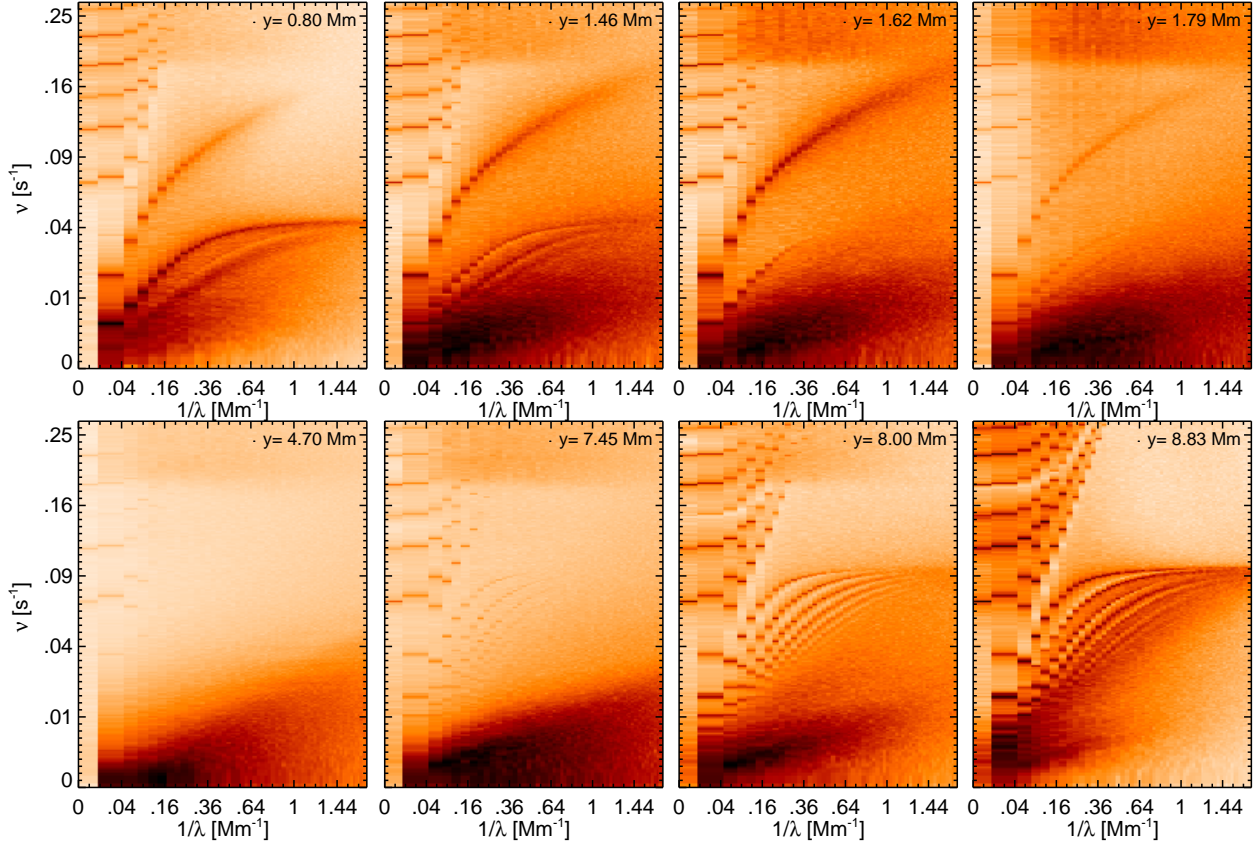
Fig. 23.— k-ω diagrams for various heights of run lc0gg. The sample heights lie in the middle of the lower stable region, just below the entropy jump, inside and above the jump (top row from left to right); in the middle of the convection zone, near the top of convection zone, at the bottom of the upper stable zone, close to the middle of this zone (bottom row from left to right).
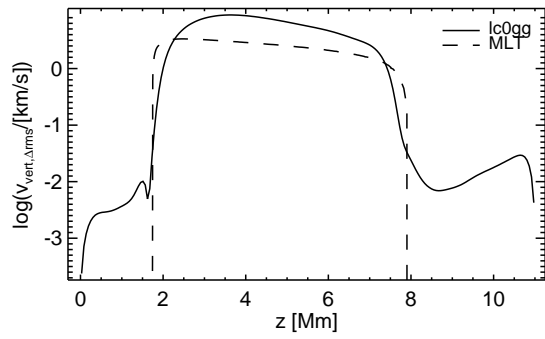
Fig. 24.— Comparison of vertical velocities derived from a hydrodynamics model (continuous lines: lc0gg) and mixing-length velocities from stellar evolution calculations (dashed lined: model 70238).

31